NTNU

Norwegian University of
Science and Technology

Simulation and Fabrication of a Photonic Crystal Transmission Filter for Biosensing Applications

Størk Lien

Problem Description

Photonic crystals are artificial materials with periodicity in the dielectric function. They can exhibit a photonic band gap, which gives them extraordinary light confining properties. Among the many potential applications of photonic crystals, biosensors for clinical use has drawn a lot of attention lately.

In this master's project, photonic crystal structures on a silicon-on-insulator (SOI) platform will be studied for use as biosensors. The eventual goal is to design and fabricate a photonic crystal transmission filter. Initially, simulations will be carried out to find appropriate designs. These will be followed by fabrication and characterization, and a partly established fabrication process will be further developed and optimized.

Simulations will be carried out using the open source softwares MIT Photonic Bands (MPB) and MIT Electromagnetic Equation Propagation (MEEP) for eigenmode analysis and finite-difference time-domain simulations, respectively.

Fabrication and characterization will be performed at NTNU Nanolab, using techniques as Electron Beam Lithography (EBL), Plasma Enhanced Chemical Vapor Deposition (PECVD) and Inductively Coupled Plasma-Reactive Ion Etching (ICP-RIE). Scanning Electron Microscopy (SEM) will be utilized for characterization. Finally, the optical performance of the fabricated devices will be tested.

Abstract

Photonic crystals are artificial materials with periodicity in the dielectric function on the sub-micron scale. They can exhibit extraordinary light confining properties superior to other known materials, making them attractive for photonic devices. Among many potential applications, the use of photonic crystals as biosensors in clinical settings has drawn significant attention lately.

In this work, photonic crystal structures are designed and simulated in two and three dimensions. The photonic crystal structure used as a basis is a hexagonal pattern of cylindrical air holes in a silicon slab. Different designs of cavity transmission filters are investigated, and the application of these filters as biosensors is investigated through simulations. Based on the simulation results, devices are fabricated with relevant nanofabrication techniques. The fabrication process of photonic devices is further optimized.

For the first time at NTNU, functioning photonic crystal transmission filters are fabricated, with quality factors of around 10^3, which is of similar order as the highest reported values for similar structures. Through simulations, the application of a biolayer to the photonic crystal surface is found to give a shift in resonance frequency that is of sufficient magnitude to be detected.

Further work could be done to improve the performance of the sensors, but the findings in this thesis support the belief in photonic crystals, and particularly transmission filters, as a promising platform for biosensing applications.

Sammendrag

Fotoniske krystaller er kunstige materialer med periodisk dielektrisitet på nanometer-nivå. De har unike lyslokaliseringsegenskaper, noe som gjør fotoniske krystaller attraktive til bruk i fotoniske komponenter og systemer. Blant de mange mulige bruksområdene har bruken av fotoniske krystaller som biosensorer i medisin fått mye oppmerksomhet de siste tiårene.

I dette arbeidet blir fotoniske krystallstrukturer designet og simulert i to og tre dimensjoner. Den fotoniske krystallstrukturen brukt som utgangspunkt er en heksagonal struktur av sylindriske hull i silisium. Ulike design av transmisjonsfiltre basert på kaviteter i krystallstrukturen blir studert, og bruken av disse som biosensorer blir utforsket ved hjelp av simuleringer. Basert på resultatene fra simuleringene blir fotoniske komponenter produsert med relevante nanofabrikasjonsteknikker, samtidig som fabrikasjonsprosessen blir kontinuerlig optimalisert.

For første gang ved NTNU blir fungerende transmisjonsfiltre basert på fotoniske krystaller framstilt, med Q-faktorer rundt 10^3. Dette er på nivå med de høyeste raporterte verdiene for liknende strukturer. Gjennom simuleringer blir det vist at påføringen av et biolag på overflaten av de fotoniske krystallene gir en stor nok forflytning av resonansfrekvensen til at det kan detekteres.

Videre arbeid kan gjøres for å forbedre ytelsen til sensorene, men funnene i dette arbeidet støtter troen på fotoniske krystaller, og spesielt transmisjonsfiltre, som lovende strukturer til bruk i biosensorer.

Preface

This master's thesis is based on work carried out during the Spring 2018, and is the final work for a degree of Master of Science in Nanotechnology at the Department of Electronic Systems (IES) at the Norwegian University of Science and Technology (NTNU). It is a continuation of a project work done during the Fall 2017, from which some results are reproduced for completeness. Parts of the theory chapter is adapted from the project work done prior to this thesis [1]. Earlier work done at IES [2],[3] have been used as inspiration, and especially the fabrication process described here builds upon this work. All the work presented in this thesis, including all figures, is carried out by the author, with one exception: The SEM image in Figure 4.8 was acquired by Ingerid Hellen.

Acknowledgements

I would like to thank my supervisor Prof. Astrid Aksnes for very helpful guidance throughout the project, for giving thorough feedback on my writing, and for always taking her time to help me and her other students. I thank my co-supervisor Jens Høvik for sharing his expertise in the cleanroom, for good scientific discussions, and for always being available for questions. Much thanks to you two, it has been a pleasure and a very positive experience to complete my masters degree.

I would also like to thank Ingerid Hellen, a fellow master student, for useful discussions and for exchanging experience from the experimental processes.

Finally, I thank my friends, family and Johanne, for being supportive through this process. Thanks to my classmates, who have made these five years at NTNU the best years of my life.

Størk Avelsgaard Lien
Trondheim, June 2018

Contents

List of Abbreviations

a-Si   Amorphous Silicon

BZ   Brillouin Zone

CMOS   Complementary Metal-Oxide-Semiconductor

c-Si   Crystalline Silicon

EBL   Electron Beam Lithography

ICP-RIE   Inductively Coupled Plasma-Reactive Ion Etching

MEEP   MIT Electromagnetic Equation Propagation

MPB   MIT Photonic Bands

PECVD   Plasma Enhanced Chemical Vapor Deposition

PhC   Photonic Crystal

PML   Perfectly Matched Layer

RI   Refractive Index

sccm   Standard Cubic Centimeters per Minute

SEM   Scanning Electron Microscopy

SOI   Silicon-On-Insulator

TE   Transversal Electric

TM   Transversal Magnetic

Chapter 1

Introduction

Motivation

Accurate and fast detection of diseases is crucial in medical diagnostics. Currently, the state of the art medical laboratories require trained personnel and expensive equipment, and it may take several hours to days to get an answer [4]. Therefore, fast and cheap sensor devices that are easy to operate are desired. One of the key properties of such devices is the ability of label-free detection, meaning that biomolecules are detected in their natural form without the need of labeling, which is laborious and time consuming. Examples on established label-free techniques are surface plasmon resonance, interferometers and optical waveguides/ring resonator structures, which utilize change of refractive index as detection mechanism [5]. They however have limitations regarding detection limit and applicability in chip-scale devices.

Photonic crystals biosensors have proven to be very promising in overcoming these limitations. Photonic crystals are artificial materials with a periodicity in the dielectric function on the sub-micron scale. They can be designed to exhibit photonic band gaps, letting some wavelengths propagate through the material, while others are prohibited. By introducing defects, it is possible to create nearly lossless waveguides and resonators with extremely high quality factors, which in turn can be used to create very sensitive biosensors. One of the main advantages of using photonic crystals for biosensing, is that light can be concentrated in small volumes, facilitating high light-matter interaction [5]. Combined with the ability to obtain very narrow resonance peaks in photonic crystal resonators, this makes it possible to create sensors that are highly sensitive to changes in the surrounding environment [6],[7]. Particularly attractive are PhC biosensors based on silicon-on-insulator (SOI) slab systems, because they are compatible with the well estab-

lished CMOS technology, and already existing and well-documented fabrication techniques can be utilized.

Objectives

Among the different possible PhC resonator designs, microcavity resonators are reported to have some of the highest sensitivities. They are also applicable in multiplexed devices, enabling detection of several biotargets simultaneously, which is considered a key property for ideal biosensors [4],[8]. Various kinds of photonic crystal cavity filters have been reported, and can be divided into two main categories: Transmission filters and drop filters, which will be defined later. This work is restricted to the study of transmission filters. A study of drop filters have been conducted in the same time period by a fellow master student.

The main objectives have been to design, simulate and fabricate a functioning transmission filter, and determine whether it is suitable for use as a sensor in the lab-on-a-chip biophotonic sensor platform under development at NTNU. In addition, an objective has been to develop and optimize processing of different types of photonic structures and devices.

Structure of the Thesis

In Chapter 2, theory of electromagnetism in periodic media and specific theory and applications of photonic crystals are presented. In addition, an introduction to relevant computational techniques and the general principles behind the fabrication techniques is given. Chapter 3 describes the methods and tools used for simulations and fabrication. In chapter 4, the findings from simulations and fabrication are presented. Since this thesis contain many different aspects in the development of photonic crystal components, and one step typically builds on the previous steps, the results are discussed as they are presented. Chapter 5 concludes the results, and topics for further research are suggested.

Chapter 2

Theory

To be able to design and simulate photonic crystal components, an understanding of the theory about electromagnetism in periodic dielectric media and photonic crystals is considered necessary. As a starting point, Maxwell's Equations are introduced, and specialized to the case of periodic dielectric media. Then, Maxwell's Equations are examined as an eigenvalue problem, similar to the Schrödinger Equation, which makes it possible to use the well-established theory of quantum mechanics and some of its results. The goal of this chapter is to introduce the reader to the most important aspects of electromagnetism in periodic media and some key properties of photonic crystals, in order to have an understanding of how the simulations are performed and how one could design optical components based on photonic crystals.

The theory presented in this chapter is based on the first chapters of Joannopoulos [9], and supported by other textbooks and articles cited consecutively.

In addition, a short section on the general principles behind the fabrication and characterization techniques used in this project is presented, including EBL, PECVD, ICP-RIE and SEM. More details on these techniques relevant for this project is presented in Section 3.3.

2.1   Photonic Crystals

2.1.1   Electromagnetism in periodic media

Maxwell's Equations

Propagation of light in a photonic crystal is governed by Maxwell's Equations:

$$\nabla \cdot \mathbf{B} = 0$$
$$\nabla \cdot \mathbf{D} = \rho$$
$$\nabla \times \mathbf{E} + \frac{\partial \mathbf{B}}{\partial t} = 0 \qquad (2.1)$$
$$\nabla \times \mathbf{H} - \frac{\partial \mathbf{D}}{\partial t} = \mathbf{J},$$

where $\mathbf{E}$ and $\mathbf{H}$ are the macroscopic electric and magnetic fields, $\mathbf{D}$ and $\mathbf{B}$ are the electric displacement and magnetic induction fields, and ρ and $\mathbf{J}$ are the free charge and current density. For this project, only *periodic dielectric media*, with no free charges and currents are considered, meaning that $\rho = 0$ and $\mathbf{B} = 0$. Furthermore, the following approximations are applied: The media considered are linear, isotropic, dispersionless and transparent. These assumptions simplify the theoretical models, and are justified in Joannopoulos [9]. Then, the following relations between $\mathbf{D}$ and $\mathbf{E}$, and $\mathbf{B}$ and $\mathbf{H}$ are obtained:

$$\mathbf{D}(\mathbf{r}) = \varepsilon_0 \varepsilon(\mathbf{r}) \mathbf{E}(\mathbf{r})$$
$$\mathbf{B}(\mathbf{r}) = \mu_0 \mu(\mathbf{r}) \mathbf{H}(\mathbf{r}), \qquad (2.2)$$

where $\varepsilon(\mathbf{r})$ is the dielectric function, $\varepsilon_0 = 8.854 \times 10^{-12}$ F/m is the vacuum permittivity, $\mu_0 = 4\pi \times 10^{-7}$ H/m is the vacuum permeability and $\mathbf{r}$ is the position. The relative permeability $\mu(\mathbf{r})$ is close to unity for most materials, and will therefore be left out. Thus the *refractive index* which in general is $n = \sqrt{\varepsilon \mu}$ will be simplified to $n = \sqrt{\varepsilon}$.

Maxwell's Equations are linear, and can therefore be separated into one spatial and one time-dependent part. For mathematical convenience, the time-dependent part is written as a complex exponential:

$$\mathbf{H}(\mathbf{r}, t) = \mathbf{H}(\mathbf{r}) e^{-i\omega t}$$
$$\mathbf{E}(\mathbf{r}, t) = \mathbf{E}(\mathbf{r}) e^{-i\omega t}, \qquad (2.3)$$

where ω is the angular frequency of the oscillating fields.

Combining the equations above with the curl parts of Maxwell's Equations and (2.2) it is possible to find an equation entirely in terms of $\mathbf{H}(\mathbf{r})$:

$$\nabla \times \left(\frac{1}{\varepsilon(\mathbf{r})} \nabla \times \mathbf{H}(\mathbf{r}) \right) = \left(\frac{\omega}{c} \right)^2 \mathbf{H}(\mathbf{r}). \tag{2.4}$$

This is called the *master equation*, because when combined with the divergence part of Maxwell's Equations, it contains all necessary information needed about $\mathbf{H}(\mathbf{r})$. For a given structure $\varepsilon(\mathbf{r})$, the master equation can be solved to find the solutions of $\mathbf{H}(\mathbf{r})$ and the corresponding frequencies, subject to the transversality requirement ($\nabla \cdot \mathbf{H}(\mathbf{r}) = 0$, which follows from the first equation in (2.1)). $\mathbf{E}(\mathbf{r})$ can then be recovered with help of Equations (2.1) and (2.2).

Approaching Electromagnetism as an Eigenvalue Problem

Equation (2.4) can be understood as an eigenvalue equation similar to the Schrödinger Equation in quantum mechanics [10], where an operator $\hat{\Theta}$ acts on the function $\mathbf{H}(\mathbf{r})$, resulting in the function itself times an eigenvalue,

$$\hat{\Theta}\mathbf{H}(\mathbf{r}) = \left(\frac{\omega}{c} \right)^2 \mathbf{H}(\mathbf{r}). \tag{2.5}$$

Here, the operator $\hat{\Theta}$ is defined as follows:

$$\hat{\Theta} \equiv \nabla \times \left(\frac{1}{\varepsilon(\mathbf{r})} \nabla \times \right). \tag{2.6}$$

Worth noticing is that $\hat{\Theta}$ is a linear operator (since taking the curl is a linear operation), meaning that a superposition of solutions to Equation (2.4) is a solution itself. Moreover, $\hat{\Theta}$ is actually a Hermitian operator, meaning that

$$(\mathbf{F}, \hat{\Theta}\mathbf{G}) = (\hat{\Theta}\mathbf{F}, \mathbf{G}), \tag{2.7}$$

which can be shown by partial integration. Here, $(\mathbf{F}, \mathbf{G})$ is the inner product of $\mathbf{F}(\mathbf{r})$ and $\mathbf{G}(\mathbf{r})$, defined as

$$(\mathbf{F}, \mathbf{G}) \equiv \int d^3\mathbf{r}\mathbf{F}^*(\mathbf{r}) \cdot \mathbf{G}(\mathbf{r}), \tag{2.8}$$

where $\mathbf{F}^*$ is the complex conjugate of $\mathbf{F}$. Again, we can benefit from the well established theory of quantum mechanics, which describes some important properties of a Hermitian operator: Its eigenfunctions have real eigenvalues, they are orthogonal, and they can be found by a *variational principle*, as will be described in Section 2.1.1.

Showing that the eigenvalues are real follows from the Hermiticity of $\hat{\Theta}$ and the definition of the inner product in Equation (2.8). Since $\hat{\Theta}$ is Hermitian we have that $(\mathbf{H}, \hat{\Theta}\mathbf{H}) =$

$(\hat{\Theta}\mathbf{H}, \mathbf{H})$. By the definition of the inner product, we get that $(\mathbf{H}, \hat{\Theta}\mathbf{H}) = (\hat{\Theta}\mathbf{H}, \mathbf{H})^*$. Recalling that the eigenvalue of $\hat{\Theta}\mathbf{H}$ is (ω^2/c^2), we now get:

$$(\mathbf{H}, \hat{\Theta}\mathbf{H})^* = (\omega^2/c^2)^*(\mathbf{H}, \mathbf{H}) = (\hat{\Theta}\mathbf{H}, \mathbf{H}) = (\omega^2/c^2)(\mathbf{H}, \mathbf{H}), \qquad (2.9)$$

from which it follows that $(\omega^2/c^2)^* = (\omega^2/c^2)$, meaning that ω^2 has to be real.

The orthogonality condition can be seen when examining the inner product of two eigenfunctions $\mathbf{H}_1(\mathbf{r})$ and $\mathbf{H}_2(\mathbf{r})$ with eigenfrequencies ω_1 and ω_2. Since $\hat{\Theta}$ is Hermitian, their inner product must be equal to zero:

$$\omega_1^2(\mathbf{H}_2, \mathbf{H}_1) = c^2(\mathbf{H}_2, \hat{\Theta}\mathbf{H}_1) = c^2(\hat{\Theta}\mathbf{H}_2, \mathbf{H}_1) = \omega_2^2(\mathbf{H}_2, \mathbf{H}_1). \qquad (2.10)$$

For $\omega_1 \neq \omega_2$, this equation requires $(\mathbf{H}_1, \mathbf{H}_2) = 0$, meaning that they are orthogonal. Two solutions $\mathbf{H}_1$ and $\mathbf{H}_2$, which from now will be called *modes*[1], can have the same frequency $(\omega_1 = \omega_2)$. They are then said to be degenerate. This phenomenon can usually be explained by symmetry in the dielectric structure. Such degenerate modes are not necessarily orthogonal.

The Electromagnetic Variational Theorem

The electromagnetic variational theorem is a method of finding the lowest energy mode, and is expressed as

$$\mathcal{U}_f(\mathbf{H}) \equiv \frac{(\mathbf{H}, \hat{\Theta}\mathbf{H})}{(\mathbf{H}, \mathbf{H})}, \qquad (2.11)$$

where $\mathcal{U}_f$ is called the *electric energy functional*. This is analogous to the quantum mechanical variational method, which is derived in chapter 7 of Hemmer [10]. It can be shown that the energy functional is minimized by the field pattern having the lowest possible frequency ω_0 (the fundamental mode, corresponding to the ground state in quantum mechanics). Writing (2.11) in terms of $\mathbf{E}$,

$$\mathcal{U}_f(\mathbf{E}) = \frac{\int d^3\mathbf{r}|\nabla \times \mathbf{E}(\mathbf{r})|^2}{\int d^3\varepsilon(\mathbf{r})|\mathbf{E}(\mathbf{r})|^2}, \qquad (2.12)$$

we see that $\mathcal{U}_f$ is minimized by concentrating the electric field $\mathbf{E}$ inside regions of high dielectric constant ε. This property is useful for understanding the qualitative features of the modes in periodic dielectric media.

---

[1]A *mode* can be described as a pattern of wave motion, where all parts of the system move sinusoidally with the same frequency [11].

Scale invariance of The Master Equation

In quantum physics and solid state physics, there are fundamental length scales beyond which we cannot relate solutions to potentials of different spatial extent. In electromagnetics there is no such fundamental length, and it's therefore possible to relate solutions of electromagnetic problems differing only by an overall contraction or expansion. This holds also for our master equation (Equation (2.4)), which is said to be *scale invariant*. For example, assuming the dielectric structure is scaled by a factor s such that $\varepsilon'(\mathbf{r}) = \varepsilon \mathbf{r}/s$, we can see what happens with the eigenfrequencies in 2.4, using $\mathbf{r}' = s\mathbf{r}$ and $\nabla' = \nabla/s$:

$$s\nabla' \times \left(\frac{1}{\varepsilon(\mathbf{r}'/s)} s\nabla' \times \mathbf{H}(\mathbf{r}'/s) \right) = \left(\frac{\omega}{c} \right)^2 \mathbf{H}(\mathbf{r}'/s). \tag{2.13}$$

Here, $\varepsilon(\mathbf{r}'/s) = \varepsilon'(\mathbf{r}')$, so the above equation becomes

$$\nabla' \times \left(\frac{1}{\varepsilon'(\mathbf{r}')} \nabla' \times \mathbf{H}(\mathbf{r}'/s) \right) = \left(\frac{\omega}{cs} \right)^2 \mathbf{H}(\mathbf{r}'/s)., \tag{2.14}$$

which is the master equation with the mode $\mathbf{H}'(\mathbf{r}') = \mathbf{H}(\mathbf{r}'/s)$ having the frequency $\omega' = \omega/s$, meaning that the solution is simply scaled by a factor $1/s$. This property is convenient when designing photonic crystal structures, as it makes it possible to test a structure at easily fabricated dimensions before scaling down to complex fabrication processes on the nano-/micrometer scale.

In this thesis, frequency and wave vectors will be expressed as dimensionless variables, since they can easily be scaled to a specific size. As we are working with periodic structures, a natural choice of scale is to choose the lattice constant a to be equal to unity, and scale other variables accordingly. In particular, the frequency and wave vector in such dimensionless (dl) units become

$$\omega_{dl} = \frac{\omega a}{2\pi c} \qquad \text{and} \qquad k_{dl} = \frac{ka}{2\pi}. \tag{2.15}$$

2.1.2 Symmetries and Solid State Physics

Continuous Translational Symmetry and Index Guiding

In the following it is convenient to express electromagnetic waves in terms of a *wave vector* $\mathbf{k}$, and for a plane wave in a *homogeneous medium* (continuous translational symmetry in three dimensions) the waves can be expressed as $\mathbf{H_k}(\mathbf{r}) = \mathbf{H}_0 e^{i\mathbf{k}\cdot\mathbf{r}}$. These waves satisfy our master equation with eigenvalues $(\omega/c)^2 = |\mathbf{k}|^2/\varepsilon$, from which we get a *dispersion*
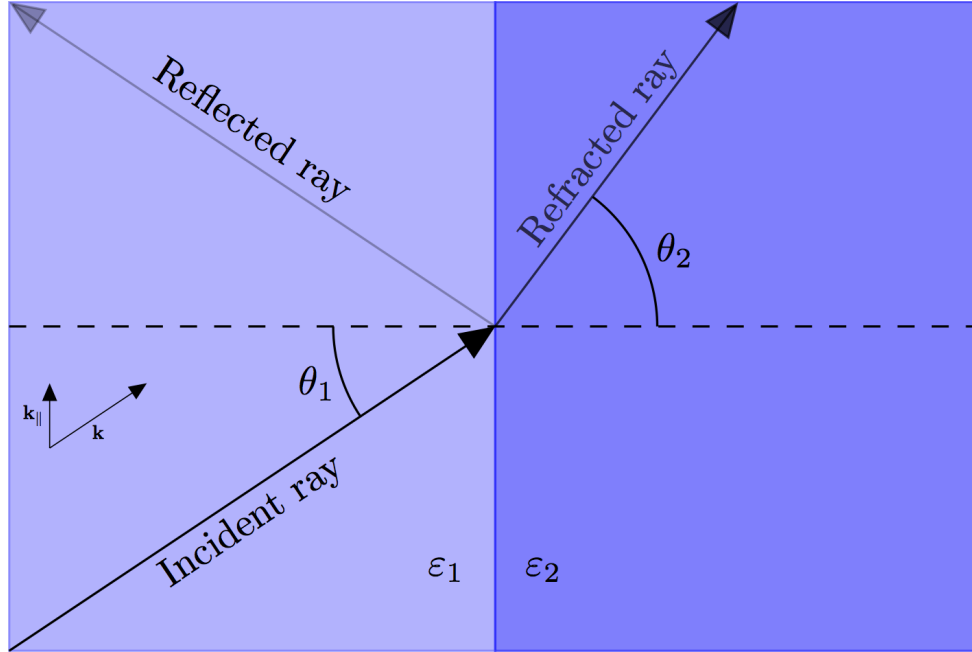
Figure 2.1: Refraction of light passing a boundary between two media of different refractive index $n = \sqrt{\varepsilon}$.

relation $\omega = c|\mathbf{k}|/\sqrt{\varepsilon} = c|\mathbf{k}|/n$. Next, we will describe waves in a medium with continuous translational symmetry in two dimensions to understand the concept of *index guiding*, which is helpful when studying waves in a *photonic crystal slab*.

Index Guiding

Consider an infinitely large plane of glass. Within the plane, there is obviously continuous translational symmetry, so the system is invariant under all translations within the plane: $\varepsilon(\mathbf{r}) = \varepsilon(z)$. The modes can be described by their in-plane wave vectors $\mathbf{k} = k_x\hat{\mathbf{x}} + k_y\hat{\mathbf{y}}$, and the waves can be written as $\mathbf{H_k}(\mathbf{r}) = e^{i\mathbf{k}\cdot\boldsymbol{\rho}}\mathbf{h}(z)$, where $\boldsymbol{\rho}$ is the position in the xy-plane. It can be understood why this a correct description of the waves by considering three points lying close together: $\mathbf{r}$, $\mathbf{r} + d\mathbf{x}$ and $\mathbf{r} + d\mathbf{y}$. Because of the in-plane symmetry, the three points should have the same magnitude of magnetic field, and could potentially only differ in their phase. But then we could distinguish different locations in the glass plane by the phase of the field, which cannot be true since we are dealing with an infinitely large plane of glass in the x-y plane. Thus, k_x and k_y must be universal, and so-called *conserved quantities.*

When a ray of light hits a boundary between two media, its behavior is usually de-

scribed in terms of *Snell's law*, visualized in Figure 2.1 (described in detail in chapter 1 of Saleh and Teich [12]). Now that we know that $k_{\parallel}$ is conserved (from the discussion above), Snell's law is obtained by setting $k_{\parallel}$ equal on both sides of the interface, using that $k_{\parallel} = |\mathbf{k}| \sin \theta = \frac{n\omega}{c} \sin \theta$. This results in Snell's law:

$$n_1 \sin \theta_2 = n_2 \cos \theta_2 \tag{2.16}$$

For $\theta_1 > sin^{-1}(n_2/n_1)$, Snell's law requires $\sin \theta_2 > 1$, which has no real solution. The perpendicular wave vectors in air become $k_{\perp} = \pm i \sqrt{k_{\parallel}^2 - \omega^2/c^2}$, corresponding to a field decaying exponentially away from the glass. Such modes are said to be *index guided.* For smaller angles θ_1, Snell's law has real solutions and we have $\omega = c|\mathbf{k}|/n = c/n\sqrt{k_{\parallel}^2 + k_{\perp}^2}$, where ω can take a continuous spectrum of frequencies above $\omega = ck_{\parallel}/n$, which is denoted the *light line.* The region of frequencies above the light line is called the *light cone.* A visualization of the light line/light cone can be seen e.g. in the band diagram in Figure 2.4(b).

Translational Symmetry and the Brillouin Zone

Characteristic for photonic crystals is that we have some kind of *discrete translational symmetry*, meaning that the crystal is invariant under certain translations. Let $\mathbf{R}$ describe a translation such that $\varepsilon(\mathbf{r}) = \varepsilon(\mathbf{r} + \mathbf{R})$. In the same way that the eigenfunctions of a wave in a periodic potential can be described by the product of a plane wave and a periodic function, this holds also for electromagnetic waves in a medium with periodicity in the dielectric structure. This is known as *Bloch's theorem*, and the waves can be written as *Bloch states* [13]:

$$\mathbf{H_k}(\mathbf{r}) = \mathbf{u_k}(\mathbf{r})e^{i\mathbf{k}\cdot\mathbf{r}}, \tag{2.17}$$

where $\mathbf{u_k}(\mathbf{r})$ represent the periodicity of the lattice and we have that $\mathbf{u_k}(\mathbf{r}) = \mathbf{u_k}(\mathbf{r} + \mathbf{R})$. Considering discrete translational symmetry in one dimension, with lattice constant a, we can see from Equation (2.17) that substituting k with $k + 2\pi/a$ gives the same function. Thus, all the information needed is contained within $-\pi/a < k \leq \pi/a$. This range of k is called the *Brillouin Zone*, and can be generalized for systems with periodicity in two and three dimensions. With this formulation of electromagnetic waves, we can finally find a way of computing photonic band structures.

By inserting Equation (2.17) into the master equation we get the following:

$$\hat{\Theta}\mathbf{H_k} = (\omega(\mathbf{k})/c)^2\mathbf{H_k}$$

$$\nabla \times \frac{1}{\varepsilon(\mathbf{r})}\nabla \times e^{i\mathbf{k}\cdot\mathbf{r}}\mathbf{u_k}(\mathbf{r}) = (\omega(\mathbf{k})/c)^2 e^{i\mathbf{k}\cdot\mathbf{r}}\mathbf{u_k}(\mathbf{r})$$

$$(i\mathbf{k} + \nabla) \times \frac{1}{\varepsilon(\mathbf{r})}(i\mathbf{k} + \nabla) \times \mathbf{u_k}(\mathbf{r}) = (\omega(\mathbf{k})/c)^2\mathbf{u_k}(\mathbf{r})$$

$$\hat{\Theta}\mathbf{u_k}(\mathbf{r}) = (\omega(\mathbf{k})/c)^2\mathbf{u_k}(\mathbf{r}),$$

(2.18)

where $\hat{\Theta}_\mathbf{k}$ is a new Hermitian operator defined as:

$$\hat{\Theta}_\mathbf{k} \equiv (i\mathbf{k} + \nabla) \times \frac{1}{\varepsilon(\mathbf{r})}(i\mathbf{k} + \nabla) \times .$$

(2.19)

This is the equation used to calculate photonic band structures in this thesis.

2.1.3 Photonic Crystals

A photonic crystal is a structure that has a periodicity of the dielectric function in one, two or three dimensions. When the periodicity is of a scale in the order of the wavelength of light, the motion of photons in the material is affected. We will start with showing that a band gap arises when sending light into a one-dimensional photonic crystal. Then the concept of band structures for two-dimensional crystals will be developed, and the importance of defects will be described. A discussion on *photonic crystal slabs* will conclude this section.

Photonic Crystal Band Gap

The origin of the photonic crystal band gap is easy to explain considering a 1D photonic crystal: A stack with alternating layers of different ε. Assume for simplicity that the layers are of equal thickness $(a/2)$, where a is the lattice constant. If the periodicity is in the $\hat{\mathbf{x}}$-direction, the primitive lattice vector for this structure is $a\hat{\mathbf{x}}$, with the corresponding primitive reciprocal lattice vector $(2\pi/a)\hat{\mathbf{x}}$. The Brillouin zone is $-\pi/a < k_x \leq \pi/a$.

Let's consider waves only with a k_x-component (waves perpendicular to the periodic structure). Assume first that the layers have the same ε. This is the same as having a continuous medium, with an arbitrarily chosen "periodicity" of a. The modes for this structure simply become $\omega(k_x) = ck_x/n$. As discussed in Section 2.1.2, k_x will be repeated outside the Brillouin zone. A way of visualizing this in a band diagram is to let the band structure "fold" back into the zone when hitting an edge, as can be seen in the left part

of Figure 2.2. If the ε of the two layers are not the same, a band gap will arise between the first and second band, when calculating the band structure from Equation (2.19). The size of the band gap increases with increasing difference in ε, as can be seen in the central and right part of Figure 2.2.
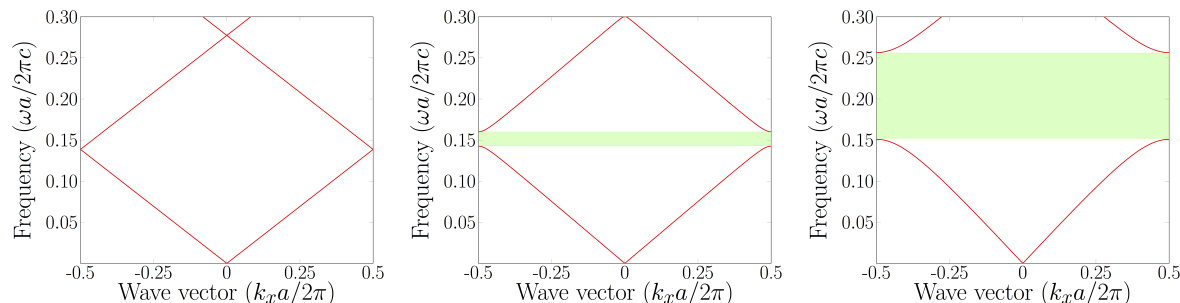

Figure 2.2: Photonic band structures for a wave propagating perpendicular to the periodicity direction of a 1D photonic crystal, with alternating layers of equal thickness of $a/2$. Left: Same ε in each layer. Center: ε alternates between 9 and 13. Right: ε alternates between 1 and 13.

The physical origin of this band gap can be understood by considering the electric field modes just above and below the gap; at $k_x = \pi/a$. For this value of k_x, the modes have a wavelength of $2a$. Such modes can be positioned in two ways: With the nodes in the high-ε material or in the low-ε material. From the discussion on the variational theorem in Section 2.1.1 we remember that modes having their energy concentrated in the high-ε layers, have lower frequency than the modes having their energy concentrated in the low-ε layers. This is explained more thoroughly when discussing the band structure for two-dimensional photonic crystals.

The size of the band gap is usually characterized by the *gap-midgap ratio* ($\Delta\omega/\omega_m$), where $\Delta\omega$ is the frequency width of the gap and ω_m is the center frequency of the gap. This is a useful way to characterize band gap sizes due to the scale invariance of photonic crystals: If the dimensions of the system are scaled up or down, the frequencies will scale accordingly, while the gap-midgap ratio stays the same.

Two-Dimensional Photonic Crystals

The structures investigated in this project are indeed 3-dimensisonal, but some of the properties can be very well approximated and described by considering a two-dimensional photonic crystal. In order to understand two-dimensional photonic crystals, the concepts Brillouin zones and reciprocal lattices in the two-dimensional case will be elaborated in
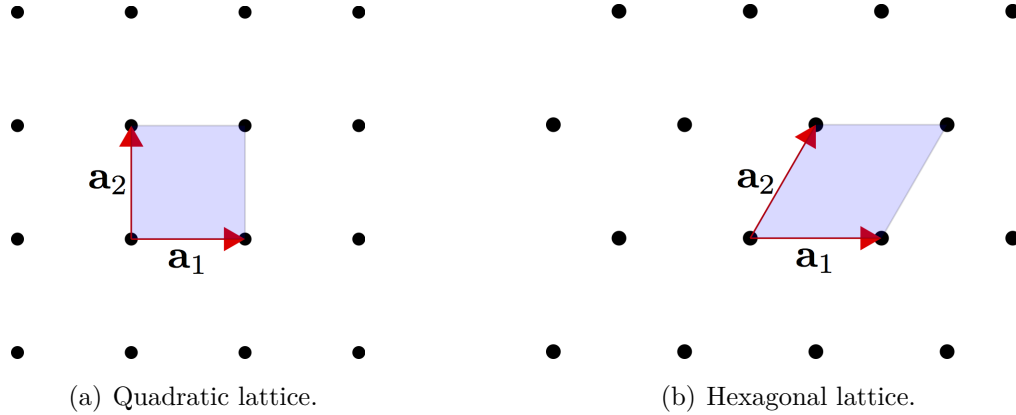
more detail in the following section.

(a) Quadratic lattice.   (b) Hexagonal lattice.

Figure 2.3: Quadratic and hexagonal lattices with lattice vectors and unit cells (shaded blue).

Two-Dimensional Crystal Structures

There are several ways to create a two-dimensional periodic structure. Each periodic structure is classified by its crystal lattice, called a *Bravais lattice*, and in two dimensions there exist five distinct periodic structures, distinguished by the symmetry operations under which they are invariant [13]. The simplest is the quadratic lattice, shown in Figure 2.3(a). Another is the hexagonal lattice shown in Figure 2.3(b). One could also make structures that are not "crystal structures" as defined in solid state physics, for example a square lattice of dielectric veins. Among the several possible photonic crystal designs, some are superior to others when considering band structure and fabrication simplicity. From this point, air will be used as the low-ε material. For the quadratic structure, it can be shown that only the option with dielectric rods in air will give a band gap, while the opposite, air cylinders in a dielectric slab, will not give a photonic band gap. For the hexagonal case, both alternatives will give a photonic band gap, but it is much simpler to fabricate air cylinders in a dielectric slab than dielectric rods in air. Therefore only such a structure will be further investigated in this project. This structure is presented in Figure 2.4(a).

The reciprocal lattice in the two-dimensional case is defined by the reciprocal lattice vectors $\mathbf{b}_j$, which are related to the real lattice vectors $\mathbf{a}_i$ by

$$\mathbf{a}_i \mathbf{b}_j = 2\pi \delta_{ij}, \tag{2.20}$$

where δ_{ji} is the Kronecker delta[2]. The *Brillouin Zone* is defined as the area in the reciprocal lattice, which is closer to one reciprocal lattice point than to any other, visualized for a hexagonal lattice in Figure 2.5.

Band Structures of Two-Dimensional Photonic Crystals

An important difference occurs in 2D photonic crystal band structures compared to the one-dimensional case. Consider the hexagonal structure of cylinders in a dielectric slab, and let the z-direction be along the cylinders. This means that the structure is invariant in this direction. Considering modes with $k_z = 0$, there are two such modes that satisfy the mirror symmetry in the xy-plane: Those with **E** in the plane and **H** normal to the plane, and those with **E** normal to the plane and **H** in the plane. The former is called *transverse-electric (TE)*, and the latter is called *transverse-magnetic (TM)*. The band structures for TE and TM modes can be very different, and a photonic band gap may occur for one polarization while not for the other. In Figure 2.4(b), a band gap for TE-
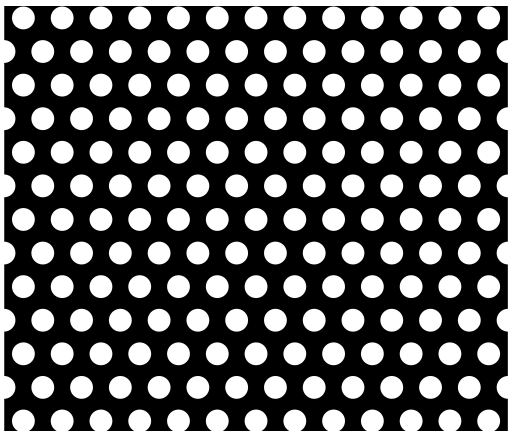
(a) Hexagonal structure of air cylinders (white) in a dielectric slab (black). The radius of the cylinders is $0.3a$, where a is the lattice constant.
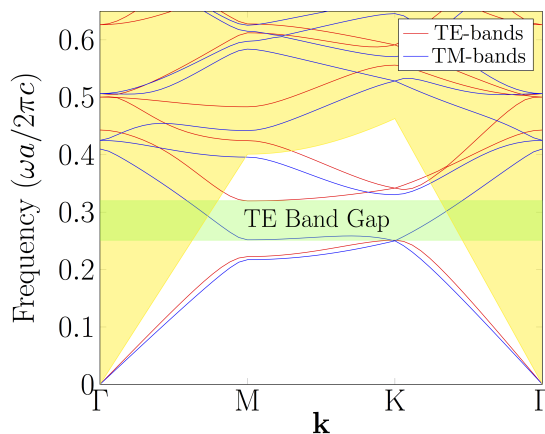
(b) Band structure for the structure in Figure 2.4(a). Frequencies are plotted as a function of **k**, when the values of **k** are varied along the irreducible Brillouin zone from Γ, to M, then to K, and back to Γ (see Figure 2.5). The yellow shade illustrates the ligt cone for a SiO$_2$ substrate.

Figure 2.4: Structure and band structure of a photonic crystal consisting of a hexagonal structure of air cylinders in a silicon slab, with hole radius $r/a = 0.3$.

---

[2]The Kronecker delta is defined as: $\delta_{ij} = \begin{cases} 1 & \text{for } i = j \\ 0 & \text{for } i \neq j \end{cases}$
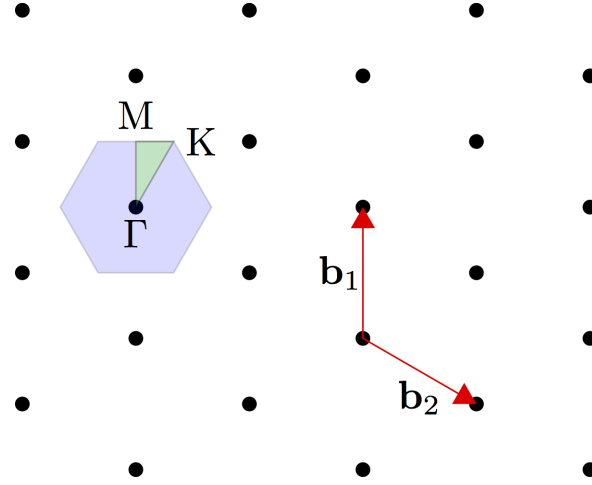
Figure 2.5: The reciprocal lattice, reciprocal lattice vectors (red) and irreducible (green) Brillouin Zone (blue) of the hexagonal lattice in Figure 2.3(b). The Γ, M and K points are located at $\mathbf{k} = 0$, $\mathbf{k} = \frac{1}{2}\mathbf{b}_1$ and $\mathbf{k} = \frac{2}{3}\mathbf{b}_1 + \frac{1}{3}\mathbf{b}_2$, respectively.

modes is observed, but not for the TM-modes. Typically, the opposite happens in a photonic crystal of dielectric rods in air. This can be understood by examining what is happening to the field components when moving across a dielectric boundary. Maxwell's Equations require the parallel component of the electric field $E_{||}$ and the perpendicular component of the *displacement field* $\varepsilon E_{\perp}$ to be continuous, as stated in chapter 5 of Saleh and Teich [12]. When moving from a higher ε_1 to a lower ε_2, the energy density $\varepsilon \mathbf{E}^2$ will decrease by a factor of $\varepsilon_2/\varepsilon_1$ if $\mathbf{E}$ is parallel to the boundary (TM-modes), and increase by $\varepsilon_1/\varepsilon_2$ if $\mathbf{E}$ is perpendicular to the boundary (TE-mode). For a structure of air cylinders in a dielectric slab, the electric field lines for the TE-modes can extend to the neighboring lattice site without crossing a boundary, since there is a continuous network of high-ε material. From the electromagnetic variational theorem 2.1.1 we can then understand that the first band ($n = 1$) will tend to concentrate most of its electric energy in the high-ε material. The next band ($n = 2$), is forced to have a node in the high-ε material due to the orthogonality requirement in Equation (2.10). Thus, some of the energy is forced into the low-ε material, causing a jump in frequency between the two first bands. This can result in a band gap for an appropriate choice of values of hole radius relative to the lattice constant. For the TM-bands however, the field lines for all bands have to cross boundaries when propagating in the material, causing a smaller frequency difference between the bands. The opposite would be the case for a structure with dielectric rods in air. A more rigorous explanation of the differences in band structures can be found in

Joannopoulos [9]. For the rest of this project, only TE-modes will be included in the band diagrams, because we are free to choose a light source with the polarization we want, and TE-bands give the most convenient band structure (with a larger band gap) for a hexagonal structure of air cylinders in a dielectric slab.

Defects in Photonic Crystals

Many interesting properties of photonic crystals arise when introducing *defects* in the crystal, that is, altering parts of the otherwise perfect photonic crystal. This can be done by changing the radius of one hole, or removing a hole completely in a structure like in Figure 2.4(a), causing a *point defect*. A *line defect* can be created by removing an entire row of cylinders. Such defects can accommodate modes that are forbidden (lie in the bandgap) in the surrounding photonic crystal structure.
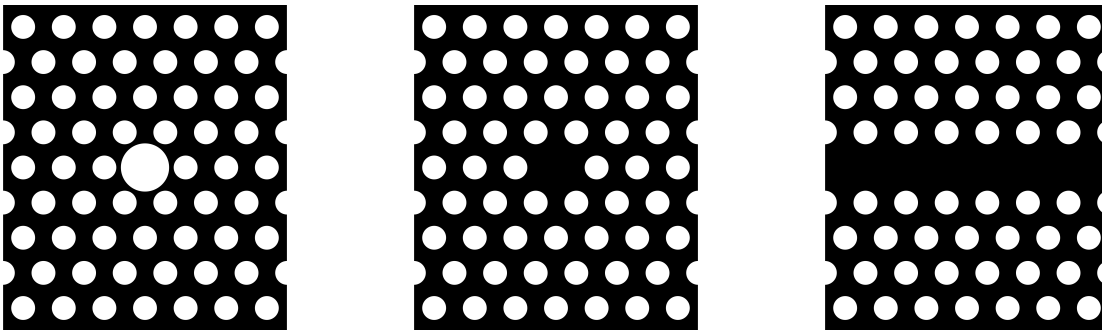
(a) Point defect by increasing the radius of a hole.

(b) Point defect by removing a hole.

(c) Line defect by removing a row of cylinders.

Figure 2.6: Point and line defects in a hexagonal structure of air cylinders in a dielectric slab.

Line Defect

By removing an entire row of cylinders, as shown in Figure 2.6(c), it is possible to support modes that are prohibited elsewhere in the crystal. Therefore, a linear defect can act as a lossless waveguide, guiding light through the photonic crystal [14]. By combining a line defect and a point defect, one can create *filters*, that allow only certain frequencies to be transmitted through the photonic crystal, while other frequencies are reflected.

Point Defect

Examples of point defects are shown in Figures 2.6(a) and 2.6(b), which we call *cavities*.

If the cavity can support a mode at a frequency within the band gap of the surrounding crystal, the mode is surrounded by reflecting walls, trapping it inside the cavity [15]. Important properties of such resonant modes are the resonance frequency ω_0, their *quality factors (Q)*, and their symmetry. The Q-factor is defined as $Q = \omega_0 \tau / 2$, where τ is the *lifetime* of the mode, defined such that the decay rate of the mode's field is $e^{-t/\tau}$.

The nature of the resonant modes depend on the size and character of the point defect. Generally, the frequency of the resonant mode increases if the dielectric constant ε decreases, as can be understood from the variational equation (2.11). Considering the band structure of e defect-free hexagonal PhC (Figure 2.4(b)), it can be understood intuitively that increasing the size of the central cavity (towards the point defect in Figure 2.6(a)) will lower the effective refractive index in the cavity compared to the surrounding crystal. Therefore, a mode of higher frequency can be accommodated in the cavity. One way to imagine this is that a mode above the band gap is "pulled" down into the band gap, resulting in a resonant mode with the mode profile shown in Figure 2.7(a). Similarly, by increasing the refractive index (for example by removing the central cavity as in Figure 2.6(b)), a mode is "pulled" up from below the band gap, giving a resonant mode with the mode profile shown in Figure 2.7(b). For each resonant mode, there is a threefold symmetry along the three symmetry axes of the hexagonal structure, meaning there are three equal resonance modes along each symmetry axis. In addition to these three identical resonances, slightly different modes can be obtained by rotating the mode profiles in Figure 2.7 by 90°. Such modes whose only difference is a 90° rotation, are in this context said to be doubly degenerate. Since the symmetry around the x- and y-axes are slightly different, the two degenerate modes might have slightly shifted resonant frequencies. When placing the point defect along a waveguide, this symmetry difference is even larger, as the photonic crystal structure is interupted along the x-direction. If the shift caused by this symmetry difference is smaller than the bandwidth of the resonance modes, the combination of the the two degenerate modes may be observed as one resonance peak, with reduced Quality factor.

In general, there is no point in trapping light if it is not possible to get it out of the cavity somehow. This can be done by placing a waveguide close to the cavity, so that the tails of the exponentially decaying fields of the resonant mode can reach the waveguide and leak out, as discussed in more detail in Section 2.1.3. Before this discussion, the concepts of photonic crystal waveguides and photonic crystal slabs will be introduced.

(a) Resonance mode "pulled" down from above the band gap, by increasing the size of the central cavity.

(b) Resonance mode "pulled" up from below the band gap, by removing the central cavity.

Figure 2.7: Resonance modes in a 2D photonic crystal consisting of a hexagonal pattern of air holes in a dielectric slab.

Photonic Crystal Slabs

Photonic crystal slabs are structures that are periodic in two dimensions, while being finite in the third. Examples of these are periodically organized dielectric rods in an "air slab", or air cylinders in a dielectric slab. While being three-dimensional structures, they resemble the properties of two dimensional photonic crystals in many ways. There are however some important differences occuring when introducing a third dimension. It allows the wave vector to have components not only within the xy-plane, but also to have a vertical component of any value in the z-direction, which produces a continuum of states, affecting the band gap.

Waveguides in Photonic Crystal Slabs

One can create a waveguide in a photonic crystal slab by changing the radius of, or removing one or more rows of cylinders. This line defect might accommodate modes that lie within the bandgap of the surrounding crystal. Since these modes are prohibited in the surrounding crystal, they will be confined within the defect, and decay exponentially into the crystal. The modes guided by this mechanism are called gap guided modes.

In addition to being gap guided, guided modes in a photonic crystal slab must also be index guided in the vertical direction, that is, they shouldn't leak into the substrate or into the air or other material at the top. Thus they have to lie below the light line as discussed in Section 2.1.2.

The band structure for a linear waveguide is found by projecting the band structure

of the bulk photonic crystal onto the band structure of the waveguide. By removing a
row of cylinders in the hexagonal structure of air cylinders in a dielectric slab, a band
structure like the one presented in Figure 2.8 arises. When a row of cylinders is removed,
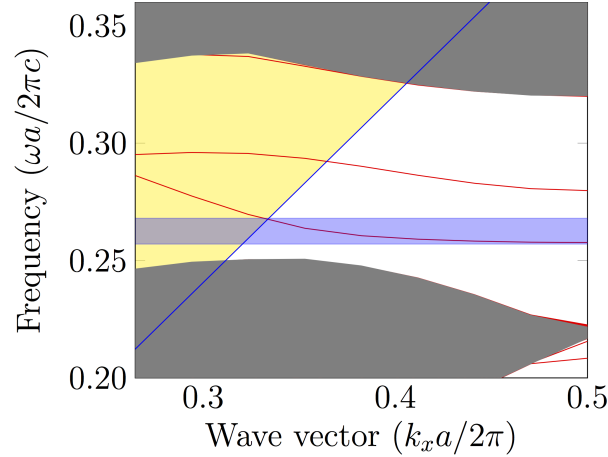

Figure 2.8: Band structure of a photonic crystal waveguide, where a row of air cylinders is
removed from a 2-dimensional photonic crystal slab consisting of a silicon slab with air cylinders
of radius $r/a = 0.3$. Gray regions represent the continuum of projected bands, and the blue line
is the light line. The yellow region represents the light cone.

the crystal only has one symmetry direction within the plane: along the waveguide. In
our case, the waveguide is in the x-direction, meaning that k_x still is a conserved quantity.
k_y is no longer conserved, so for any k_x, there exist a continuum of possible values of
k_y. By projecting all those combinations of states in the bulk crystal onto the symmetry
direction of the waveguide, the gray regions in Figure 2.8 arise. The practical procedure
for obtaining this band structure is described in more detail in Section 3.2.3.

From the band structure in Figure 2.8 it is evident that modes exist within the bandgap,
and the parts of the modes that are also below the light line are both gap guided and
index guided. Several requirements have to be met for a functioning photonic crystal slab
waveguide:

- There must exist modes covering the frequency length of interest.

- These modes must also be index guided (lie below the light line).

- There should be no leaky modes (inside the light cone) at the same frequencies.

To optimize the performance of the waveguide, one should also have the following consid-
erations in mind:

- A larger bandgap will better confine guided modes.

- The modes that lie near the middle of the band gap are better confined.

- A larger dispersion (larger slope) of the guided modes' bands below the light line will result in a broader transmission spectrum.

All these aspects can't always be optimized at the same time. Compromises might have to be made, ensuring that the most fundamental requirements are met and the less important parameters are as good as possible.

Photonic Crystal Transmission Filter

The term *filter* is used for a structure that transmits or redirects certain wavelengths while reflecting the others. A *drop filter* is able to "pick out" certain wavelengths from a waveguide, and to "drop" them into another waveguide [16]. A *transmission filter* can transmit certain wavelengths while reflecting the others [17], and this kind of filter is the focus of this thesis.

By placing a point defect like the ones in Figure 2.6 inside a waveguide, one can create a transmission filter, that transmits a narrow band of wavelengths, while reflecting others. This can be motivated intuitively: near the resonance wavelength, light can couple from the input waveguide into the cavity, which again can couple to the output waveguide. In order to describe this phenomenon in more detail, *temporal coupled-mode theory* will be introduced.

Temporal Coupled-Mode Theory

Temporal coupled-mode theory is based on conservation of energy in a system with idealized components (for example waveguides and cavities), that are coupled to each other. A transmission filter can be represented by an input waveguide, a resonance cavity and an output waveguide, as in Figure 2.9.

The cavity has a resonance frequency ω_0, and the resonant mode decays with lifetimes τ_1 and τ_2 into the input and output waveguides, respectively. Due to the symmetry of the structure, the lifetimes must be equal ($\tau_1 = \tau_2$). In order to simplify the problem it is necessary to assume *weak coupling*[3]. This can be ensured by surrounding the cavity by sufficient periods of the photonic crystal in the direction of the waveguide. Let A be

---

[3]In the weak coupling limit, the decay rates (determined by the lifetimes) is the dominating mechanism for the interaction between the cavity and the waveguides [18] and [19].

the amplitude of the fields in the cavity, and $|A|^2$ the energy stored in the cavity. Let $S_{l\pm}$ be the amplitude of the modes in the waveguides going towards and away from the cavity, where $l = 1, 2$ for the input and output waveguide, respectively, as illustrated in Figure 2.9. $|S_{l\pm}|^2$ is then the power of the waveguide modes. Due to the weak coupling assumption, the cavity mode will decay exponentially as if there were no incident power from the waveguides. The total lifetime is given by $1/\tau = 1/\tau_1 + 1/\tau_2$, which gives the following time-evolution of A: $A(t) = A(0)e^{-i\omega_0 t - t/\tau}$. Including the energy going into and out of the waveguides, the two equations describing the system become:

$$\frac{dA}{dt} = -i\omega_0 A - A/\tau_1 - A/\tau_2 + \alpha_1 S_{1+} + \alpha_2 S_{2+} \tag{2.21}$$

$$S_{l-} = \beta_l S_l + \gamma_l A, \tag{2.22}$$

where α_l and γ_l are constants representing the coupling strength, and β_l is the reflection constant. In the weak coupling limit, these constants approach $\beta_l \to 1$ (100% reflection), $\alpha_l = \gamma_l = \sqrt{2/\tau_l}$. The transmission of such a filter is obviously $T(\omega) \equiv |S_{2-}|^2/|S_{1+}|^2$, which can be expressed as:

$$T(\omega) = \frac{4/\tau_1 \tau_2}{(\omega - \omega_0)^2 + (1/\tau_1 + 1/\tau_2)^2}, \tag{2.23}$$

which is the equation for a *Lorentzian spectrum*, centered around $\omega = \omega_0$. For such a spectrum, $1/Q$, where Q is defined as $Q = \omega_0 \tau/2$, is exactly equal to the fractional width $\Delta\omega/\omega_0$ at half maximum, and Q can be expressed as $Q = \omega_0/\Delta\omega$. Q is commonly referred to as the *quality factor* of the resonance. A transmission spectrum can be obtained by analyzing the electromagnetic power coming out of the second waveguide.

2.1.4   Biosensing

Biosensing is a general term for transferring the presence of biomolecules into some kind of measurable signal by the help of an appropriate transducer. Several types of sensing
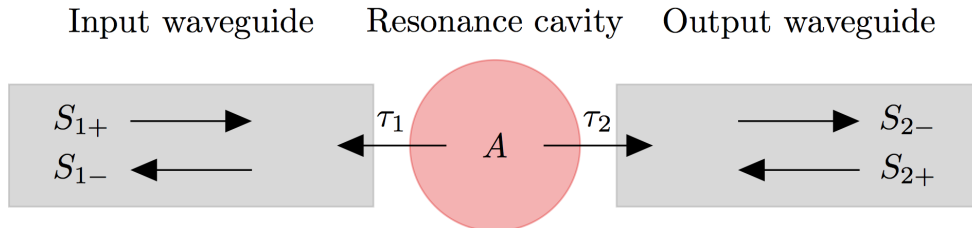
Input waveguide   Resonance cavity   Output waveguide

Figure 2.9: Transmission filter represented by idealized components.

mechanisms exist, the most common are based on optical, electrochemical or mass-related transduction [20]. Within the branch of optical biosensors, two main catagories exist: Label-free and fluorescent biosensors. The latter relies on labeling the biomolecule with fluorescence emitting tags, which is a laborious process and might affect the measurand, but provides very good sensitivity. With label-free detection, biomolecules are detected in their natural form, and such detection can be quick and cheap. Several detection mechanisms are used, but only refractive index measurements will be included here.

The presence of biomolecules on a surface will alter the refractive index, and this build-up of target molecules can be enhanced by immobilizing specific binding agents on the surface. The theory behind this is complex, and only the very basic concepts are included here. As shown in Figure 2.10, binding agents are immobilized on the surface, for example the inside if the cylinders in a photonic crystal slab. In the presence of the relevant target molecules, a biolayer will form on the surface, causing an increase of refractive index compared to the buffer solution. This RI-change is expected to cause a redshift in resonance frequency of a transmission filter. Immobilizing binding agents on the walls of the cylinders in a photonic crystal slab might be a difficult process. An alternative is to functionalize only the top of the slab, as this might also cause a shift of the resonance frequency.
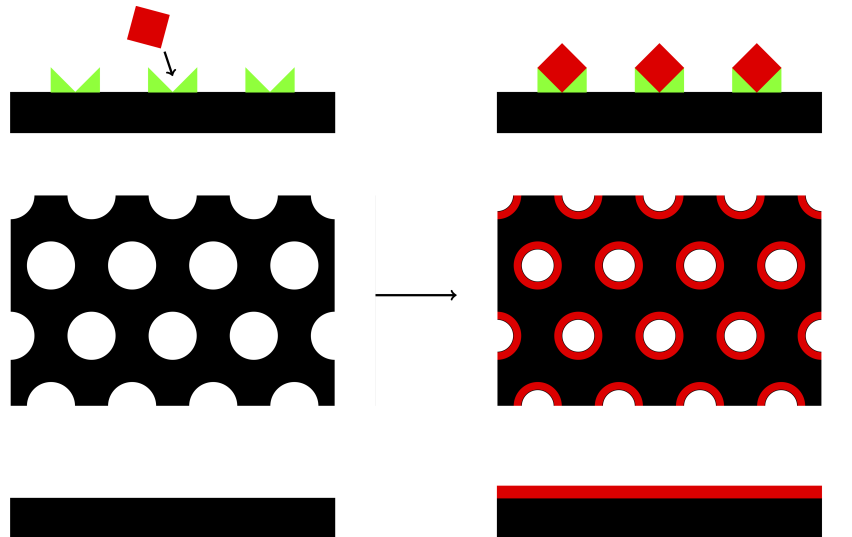

Figure 2.10: Binding of target biomolecules (red) to binding agents (green) immobilized inside the cylinders and on the surface of a photonic crystal slab.

2.2   Simulations

2.2.1   Computational Methods

In order to calculate band diagrams, transmission spectra and field patterns, it is necessary to approximate solutions of Maxwell's Equations numerically. This has become possible over the last few decades due to rapid development of computational power, followed by the development of sophisticated numerical methods. When dealing with photonic crystals, different computational problems have to be solved, and for this project, mainly two different problems arise, which are *frequency-domain eigenproblems* and *time-domain problems*.

Frequency Domain Eigenproblems

This is the kind of problem that has to be solved when we want to find band structures $\omega(\mathbf{k})$ and fields in a system, as described in Section 2.1.2. This is done by solving Equation 2.19, which only has to be done for a single unit cell since $\mathbf{u}_k$ is periodic. When solving this equation numerically, it has to be discretized into a finite number of unknowns. This can be done using the *plane-wave expansion* method [21], in which a periodic function is approximated by a Fourier series (a finite sum of sines and cosines), which can be solved by standard algebraic methods. Another approach is to solve only for the lowest eigenvalues, since the relevant information about the band structure is usually contained in the first few bands. Such a method can be developed from the electromagnetic variational theorem presented in Section 2.1.1.

The methods described above are appropriate when dealing with periodic structures. For non-periodic structures, such as waveguides and point defects, such methods don't work. In such cases, a *supercell approximation* can be used, in which the structure is made periodic with a large computational cell surrounding the defect. The reason this is a good approximation is the fact that the fields are concentrated in the waveguide, and decay exponentially into the surrounding photonic crystal.

Time-Domain Simulations

For other kinds of problems, such as when sending a pulse of light into a material, it is interesting to know how the fields evolve in time. For such problems, *time-domain* simulations have to be carried out. The most common time-domain technique is the *finite-difference time-domain (FDTD)* method, in which space and time are divided into

grids of discrete points, and the derivatives of time and space in Maxwell's Equations are approximated by finite differences [22]. The FDTD method is used for finding transmission spectra of the transmission filters presented later in this thesis.

FDTD versus FEM

A common method for solving frequency domain problems is the Finite Element Method (FEM), in which space is divided into smaller (finite) elements [23]. A strength of this method is the ability to adjust the element sizes depending on the complexity of the geometry. When analyzing the evolution of an electromagnetic field in a material, both FEM and FDTD can be used. FDTD computation time depends on the number of time steps that are carried out, which again depends on the frequency width of the source: The larger the frequency range, the shorter the computation time. FEM computation time is determined by the number of frequencies needing to solve for. Therefore, for a wide frequency spectrum, FDTD should be used, and for a narrow spectrum, FEM would be more efficient.

2.3 Materials, Fabrication and Characterization

In this section, the general principles behind the methods for fabrication and characterization are presented. More details and parameters relevant for this specific project is given in Section 3.3. A discussion on the materials used is also included.

2.3.1 Silicon-On-Insulator (SOI)

The silicon-on-insulator (SOI) material configuration, consisting of Si on top of SiO_2, has become an attractive platform for compact photonic devices over the last decades. Three important reasons why SOI is suitable for this purpose are often pointed out: Firstly, crystalline silicon has excellent optical properties for wavelengths above 1200 nm, with very low absorption, making it suitable for the well established telecommunications technology which uses wavelengths around 1550 nm. Secondly, due to high RI contrast between Si and SiO_2 small waveguide cross-sectional area while still facilitating single-mode operation is possible [24]. Therefore, very compact devices can be made. Thirdly, photonic devices based on SOI can be fabricated with the techniques already available from the well established CMOS technology [25].

A common choice of silicon thickness is 220 nm, because it supports only a single slab mode at frequencies around 1550 nm [26]. With this thickness, a rectangular waveguide should have a maximum width of around 520 nm, to satisfy the single-mode condition, ensuring better confinement and avoiding problems related to different dispersion between several modes [25],[27]. In fact, two modes are supported with this geometry, one of each polarization (TE and TM), but as the TE mode has the most convenient properties in the context of photonic crystals, as stated in Section 2.1.3, and the TE mode is much better confined [27], this is the mode of interest. The TE mode has sufficiently low leakage with an oxide layer of around 1000 nm, which therefore is an oxide thickness commonly used.

Crystalline silicon (c-Si) is the best choice regarding optical properties of an SOI waveguide. It is however expensive due to a complicated fabrication process. Therefore, amorphous silicon (a-Si) has become a promising candidate. It can be grown cheap and easy with PECVD on a cheap thermally oxidized silicon wafer. c-Si has losses typically around 1 - 2 dB/cm[25]. High quality a-si is reported to have losses as low as 2.3 dB/cm at 1550 nm [28], making it a good substitute for c-Si, at least for research purposes. Due to the lower costs, and sufficient quality in photonic devices, a-si deposited with PECVD on a thermally oxidized silicon wafer is the material choice in this project.

2.3.2   Plasma Enhanced Chemical Vapor Deposition

Plasma Enhanced Chemical Vapor Deposition (PECVD) is a technique used to deposit thin films of various materials on a substrate. Gas precursors are introduced into a vacuum chamber, where a strong electromagnetic field is applied to excite the the gas precursors into a plasma[4]. Compared to conventional CVD, which requires high temperatures to initiate the chemical reactions, PECVD can be operated at lower temperatures, since the plasma ensures sufficient reactivity of the gas precursors [30].

PECVD of a-Si

When depositing a-Si with PECVD, silane gas(SiH_4) is used as the source of silicon. Argon is used as an inert gas for modifying the plasma, and also improves the surface uniformity of the deposited silicon [31]. The processes involved during PECVD are complex, and will be simplified to the net chemical reaction equations in this thesis. The relevant chemical

---

[4]A plasma is a highly ionized gas, considered the fourth state of matter. It is created either by high temperatures or electromagnetic fields knocking electrons off the atoms, leaving positively charged and reactive atoms [29].

reaction present when depositing a-Si from silane is:

$$\mathrm{SiH_4(g) + Ar(g) \longrightarrow Si(s) + 2\,H_2(g) + Ar(g).} \tag{2.24}$$
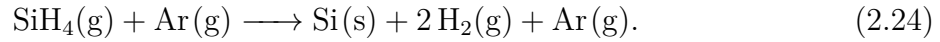
Further details on the amounts of precursors and other parameters used during the deposition is presented in Section 3.3.

2.3.3 Electron Beam Lithography

Electron Beam Lithography (EBL) is a lithography technique in which an electron beam is utilized to pattern an electron-sensitive film, called a resist. The resist usually contains organic polymers, and when exposed to the electron beam, the solubility of the resist will change. When exposed for a chemical solution (developer), the regions of the film with higher solubility are removed. The patterned resist can then be used as an etching mask for transferring the pattern to the underlying substrate.

Resist Patterning

There are two main types of resists used in EBL, as for other types of lithography. A *positive* resist experiences fragmentation of the polymer chains upon electron-radiation, making the exposed areas more soluble. After development, only the unexposed areas of the film are left. A *negative* resist experiences cross-linking upon e-beam exposure, increasing the solubility. Therefore, only the exposed areas are left after development. The pattern transfer for positive and negative resists is visualized in Figure 2.11.

An important factor in an EBL exposure is the resist sensitivity and the exposure dose used. This relies on many factors, such as the chemical composition of the resist, the amount and characteristics of the electron scattering in the resist and the substrate, and the development process. All these factors have to be taken into account when determining electron doses for the process.

Instrumental Setup

A typical EBL setup is very similar to that of an SEM. An electron source is mounted on top, producing an electron beam which travels through several lenses, deflectors, a beam blanker, stigmators, and an aperture before hitting the sample [32]. The purpose of the beam deflectors is to scan the electron beam across the sample, within what is called a *write field*. The beam blanker is necessary to turn off the beam while moving the sample

from one write field to another. The aperture is used to limit the convergence angle of the beam. Due to imperfections in the beam column, astigmatism may occur, meaning that the shape of the focused electron beam becomes elliptic and not circular, as it should ideally be. Therefore, stigmators are vital to correct for this effect, so that the exposure dose becomes as calculated for a circular beam spot. The sample is mounted on a stage which has a very precise mechanical system for accurate positioning of the sample, which can move the sample around during exposure.

Strengths and Limitations

Compared to photolithography, in which the resolution is limited by the wavelength of light, much better resolution is possible with electrons as radiation source. This is due to the much smaller wavelength of electrons. There are however other factors limiting the resolution of EBL, the most prominent being electron scattering. When using a beam size as small as for example 1.8 nm, the minimum line width possible is around 7 nm in a typical EBL system of today [33].

Being a direct writing technique, where the electron beam has to be scanned across the entire pattern, EBL has a low throughput compared to photolithography. Thus it is not suitable for high-volume fabrication. Therefore its main applications is fabrication of photomasks, low-volume production and research and development.
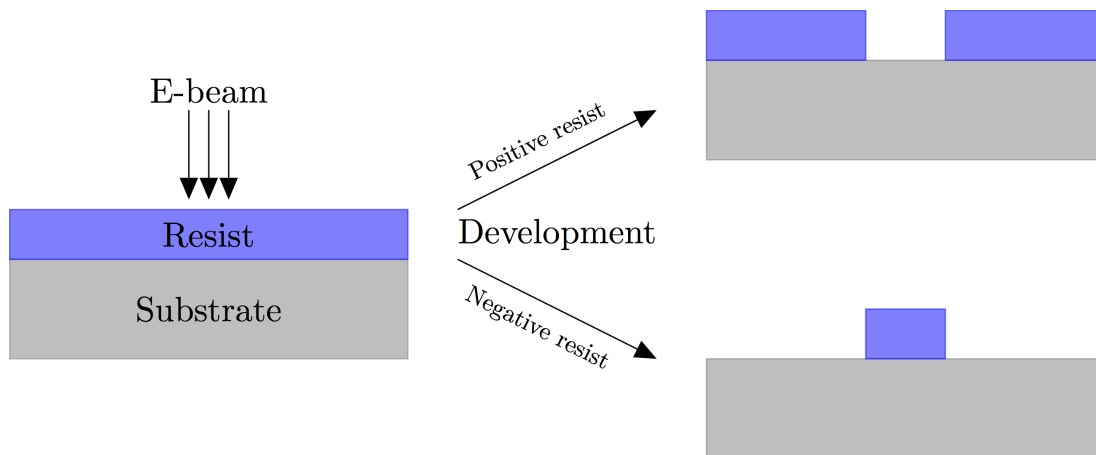

Figure 2.11: Schematic of how negative and positive electron resists are patterned during exposure to an electron beam and a following development.

2.3.4 Inductively Coupled Plasma-Reactive Ion Etching

Reactive Ion Etching (RIE) is a commonly used dry etching technique in the semiconductor industry. An electromagnetic field is used to create a plasma of reactive ions. A negative (DC) bias is applied to the lower electrode, on which the substrate is placed. This causes the positively charged plasma atoms to accelerate towards the substrate, where they react both chemically and physically by transfer of kinetic energy. Different kinds of RIE reactors exist, one of the most common being Inductively Coupled Plasma (ICP) reactors. In ICP reactors, an additional electromagnetic field is applied independently of the dc bias, by which the inlet gas is ionized away from the substrate. It is therefore possible in ICP reactors to control the plasma and the DC bias independently of each other. This is considered the main advantage of ICP-RIE compared to other reactors, for example Capacitively Coupled Plasma (CCP), where there is only one source of electromagnetic field accounting for both the plasma generation and the acceleration of ions towards the surface. This independence, combined with the many possible combinations of etching agents, allows for fine tuning of etch parameters to obtain the desired etching action for many different materials [34].

Etching Action and Etch Profile

Both physical etching (from the kinetic energy of the ions) and chemical etching (from free radicals and charged ions in the plasma) are present in a RIE process. The relative impact of physical and chemical etching mechanisms can be tuned to a large degree in an ICP-RIE. By increasing the ICP power, the degree of ionization will increase, favoring chemical etching. By increasing the DC bias to the lower electrode, the momentum of the incoming ions will increase, favoring physical etching. Strongly related to the etching mechanisms is the etch profile. Physical etching causes *anisotropic* profiles (straight sidewalls), while chemical etching causes *isotropic* profiles (rounded sidewalls).

Selectivity

An important parameter in all etching processes is the selectivity, which is defined as the etch rate of two materials etched under the same conditions. It is normally desired to etch only one material (the substrate) while having minimal etching of the mask (typically a resist). The selectivity between the substrate and resist sets the limit of how thick the resist layer needs to be.

2.3.5   Plasma Cleaning

Plasma cleaning is a process for removing tiny amounts of contaminants that are present on all surfaces. These contaminants may be there as a result of earlier process steps, such as resist development, cleaning, or just from being exposed to the surroundings for some amount of time. Removal of these contaminants is important for the quality of further processing steps, such as deposition and etching. There are often hydrocarbons left on a surface after a processing step, which may affect the quality of subsequent steps. These can be removed in an oxygen plasma, which is typically accompanied by UV light, in a vacuum chamber. The combination of UV light, ions and radicals split up longer chains of hydrocarbons. The shorter, fragmented parts become gaseous in the low-pressure atmosphere, and are removed by suction. It is crucial that the next processing step is done immediately after plasma cleaning, as contaminants from the surroundings will build up gradually.

2.3.6   Scanning Electron Microscopy

Scanning Electron Microscopy (SEM) is a popular technique for high resolution imaging. By using electrons instead of light, the fundamental resolution limit of optical microscopy (around $\lambda/2$) is overcome, and images with resolution down to $1\,\mathrm{nm}$ can be obtained [35].

A focused electron beam is scanned over the surface to be investigated, causing several kinds of interactions with the atoms in the surface. Some electrons are scattered back after colliding with the surface atoms, referred to as backscattered electrons. Other electrons are dislodging electrons in the material, referred to secondary electrons. In addition, X-rays are created from the collisions. The different signals can be detected and give information about the surface topography and material composition.

Secondary electrons arise from inelastic collisions with the incident electrons. They typically have low energy, and only those near the surface are able to escape. This means the SE mostly give information about the surface topology.

Backscattered electrons (BSE) are elastically scattered back from the substrate. Since they are elastically scattered, they have more energy than the secondary electrons, and can escape from deeper in the substrate. This causes a reduction in the resolution, but can give information in what is deeper in the substrate. In addition, the scattering process is highly dependent on the atomic number of the atoms in the substrate, meaning that the BSE give higher elemental contrast than the SE.

Chapter 3

Experimental Methods and Procedure

3.1 Numerical Software

The numerical software used in this project is MIT Photonic Bands (MPB) and MIT Electromagnetic Equation Propagation (MEEP), which are both developed at Massachusetts Institute of Technology (MIT). They are both operating with dimensionless units, which as discussed in Section 2.1.1 is convenient when researching photonic crystals, as properties are scaled up and down as the physical sizes scale - it is only the relative sizes in the dielectric structures that matter.

3.1.1 MIT Photonic Bands (MPB)

MPB is an open source software package for computing eigenstates of Maxwell's equations in periodic dielectric materials. It is suited for calculating dispersion relations and eigenstates for structures such as strip waveguides, optical fibers, and especially photonic crystals, for which it was particularly designed [36].

MPB uses the frequency-domain method, meaning that it computes the eigenstates and eigenvalues of Maxwell's equations directly, which is the best suited method for calculating band structures. More details on how the simulations are run is given later in this chapter. An example code is given in Appendix A.

3.1.2   MIT Electromagnetic Equation Propagation (MEEP)

MEEP is an open source software package implementing the finite-difference-time-domain (FDTD) method to simulate propagation of electromagnetic waves. The input is a dielectric structure in one, two or three dimensions in addition to a current source. The simulations space is divided into a discrete grid, and the evolution of the electromagnetic fields is computed using discrete time steps. As the grid in space and time gets finer and finer it becomes closer to the real continuous equations. *Perfectly matched layers* (PML) [37], that absorb all incoming fluxes, are applied to all outer boundaries. This allows simulating over finite structures, as it avoids reflection at the boundaries.

All transmission spectra in this thesis are computed with MEEP. More details and an example code of how a simulation of a transmission filter is set up is given in Appendix B.

Harminv

Harminv is an additional program used with MEEP, also developed at MIT, that is used to find resonances and to compute their Q-factors [38]. This is done by *harmonic inversion of time signals* [39], which is solved by the *filter diagonalization method*. A rigorous explanation of this technique falls beyond the scope of this project, more details can be found in Mandelshtam et al. [39] and Taflove et al. [40].

3.2   Simulations

The structures studied in this project are photonic crystals consisting of a hexagonal pattern of air cylinders in a layer of silicon on top of silicon dioxide. Thickness of the silicon layer is 220 nm, which has been shown to be an appropriate thickness for satisfying the single-mode condition, as explained in Section 2.3.1. Testing of the fabricated devices was done in air environment, so the simulations were done with optical constants belonging to air as the "medium" in the cylindrical holes and in the surroundings. As the eventual application of these devices are biosensing, more specifically blood analysis, some simulations were also carried out in an aqueous environment, substituting air with the optical constants of water.

Initially, simulations of band structures in two dimensional photonic crystals were done, to find a suitable PhC structure. Next, these were expanded into simulations of PhC waveguides, which were done in parallel with simulations of different transmission

filters, to find a functioning structure. Three dimensional simulations were done for the most promising waveguide and transmission filter parameters. Finally, simulations were performed to study the effects on the resonance frequency when introducing a biolayer on the transmission filters.

3.2.1 Effective Refractive Index Approximation

Due to 3D simulations being expensive in terms of computational power and time, 2D simulations were performed for initial tuning of parameter. Light propagating in a silicon slab as thin as 220 nm on top of SiO_2 surrounded by air, will experience a different refractive index than in bulk silicon. Therefore, in order to carry out 2D simulations, the *effective refractive index* was found. This was done by a modal analysis in COMSOL [41], for electromagnetic radiation of wavelength 1550 nm. The values for the refractive indexes of each material were acquired from the Refractive Index Database [42]. These are displayed in Table 3.1, together with the thicknesses of each layer used in the simulation. Figure 3.1 illustrates the simulation geometry.

Table 3.1: Refractive index and thickness of the different layers used in the simulation of the effective refractive index in an SOI slab. The RI values are acquired from The Refractive Index Database [42].

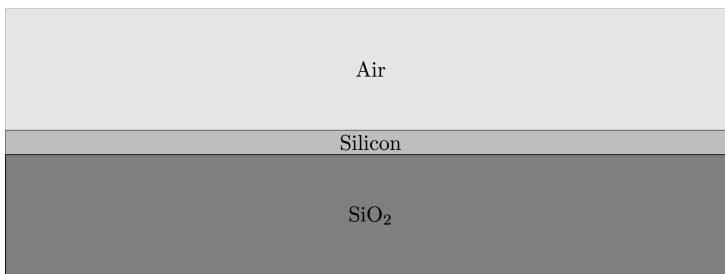| Layer	Refractive Index	Thickness [nm]
SiO_2	1.44	1000
Silicon	3.48	220
Air	1.00	1000

Figure 3.1: Simulation geometry for finding the effective refractive index of an SOI slab.

3.2.2   Photonic Crystal Structural Parameters

The choice of structural parameters of the photonic crystal, like the lattice constant a, the hole radius r and the slab height h has a huge impact on the performance of the final device. Therefore, the band structure of bulk PhCs are investigated initially, continued by the study of PhC slabs. Next, the band structure and transmission characteristics of PhC waveguides are studied before proceeding with transmission filters, both the latter in two and three dimensions.

Hole Radius

Band structures for bulk photonic crystals were computed with MPB, to investigate the relation between the band gap size and the radius of the cylinders. After obtaining several band diagrams, it became evident that the extreme values of the bands occur at the M and K-points. The simulations were for simplicity therefore performed at these points only. The mesh size (the size over which the dielectric constant is averaged) is set to $a/16$, and the resolution (number of pixels per lattice parameter) is set to 128.

3.2.3   Linear Defect Waveguide

The band structures of guided modes in a linear defect waveguide were investigated next. Band diagrams were computed with MPB by projecting the k-vectors of the defect-free PhC onto the translational symmetry direction of the linear defect PhC. From the definition of the Brillouin zone in Section 2.1.2, the direction of the linear defect waveguide corresponds to the M-direction in the reciprocal lattice. A computational cell of the defect-free PhC with dimension 1×25 was used to find the bands to project onto the translational symmetry direction of the linear defect. In such a computational cell, the bands fold back into the Brillouin zone, producing a quasi-continuous set of bands, which would approach a continuum in the limit of an infinite computational cell. Next, the band diagram of the linear defect PhC was computed, by using a similar computational cell, but with a missing cylinder in the middle. The two band diagrams were then combined, and the light line for the SiO_2 substrate was included, to produce the complete band diagram for the linear defect waveguide. The computational cells are illustrated in Figure 3.2. These simulations were done with a mesh size of 3 and a resolution of 32, as defined in the previous section. An example code of a simulation of a PhC waveguide and some more details regarding the simulations can be found in Appendix A.
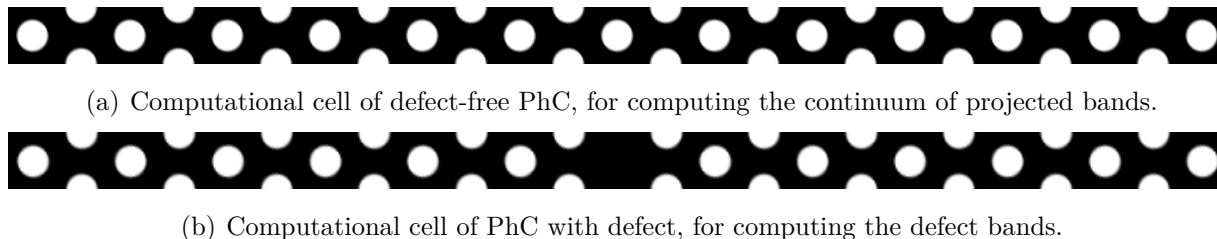
(a) Computational cell of defect-free PhC, for computing the continuum of projected bands.

(b) Computational cell of PhC with defect, for computing the defect bands.

Figure 3.2: Computational cells used for computing the band structure of a linear defect PhC waveguide with MPB.

The band structures of the guided modes in linear defect waveguides were investigated with varying r/a-ratio, in order to find a structure able to guide the wavelengths of interest. These were accompanied by FDTD simulations of the transmission through the waveguides with MEEP. Both two- and three-dimensional simulations were carried out. Unfortunately, when performed on a personal laptop, the 3D simulations proved to be very time consuming when done with high resolution and for big structures. Attempts on high resolution simulations of 3D structures resulted in the computer crashing halfway through the simulation. 3D simulations were therefore carried out with a grid resolution of only $a/16$ and a mesh size of 3. The length and width of the PhC waveguide simulated were 17 and 15 lattice periods, respectively.

When performing three-dimensional simulations, the bottom oxide layer needs to be specified in terms of refractive index and thickness. The thickness of the silicon slab also needs to be specified, in addition to the actual refractive index. The refractive indexes are acquired from [42], and summarized in Table 3.2 together with physical and relative (dimensionless) thicknesses. The real SOI samples used during fabrication have an oxide thickness of 1000 nm and a silicon thickness of 220 nm, but for computational simplicity, an oxide layer exactly 4 times as thick as the silicon layer (880 nm) were used in the simulations. Also, the top "layer" of air was set to 880 nm. This should not affect the results much, as the electromagnetic fields are highly confined in the silicon layer by total internal reflection, and decay exponentially into the substrate.
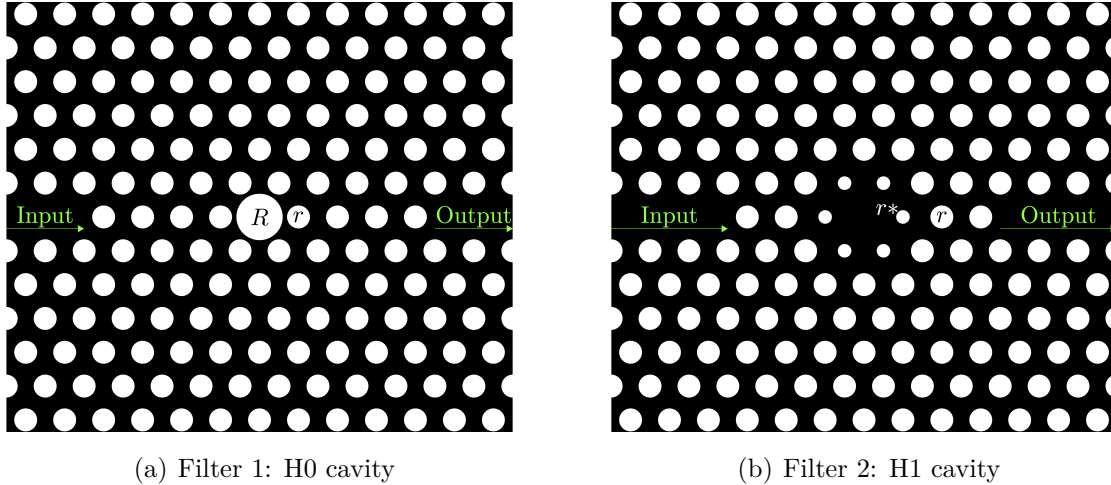
3.2.4 Transmission Filter

Two different designs of transmission filters were studied. There are many different filter designs that have been reported, but as no functioning PhC transmission filters yet had been fabricated in our research group, the idea was to start with simple designs. In

Table 3.2: Physical and relative thickness, and refractive index of the layers in the simulated slab systems.

Layer	Physical thickness [nm]	Relative thickness	Refractive index
Oxide	880	2.164	1.44
Silicon	220	0.541	3.48
Air	880	2.164	1.00
Water	880	2.164	1.33

addition, as one of the objectives of our research group is to fabricate a multiplexed filter (multiple filters combined to allow for testing of different biomarkers simultaneously), a simple and small design where the resonance frequency can be shifted by simple adjustment of geometrical parameters would be beneficial. This is the case for both filters investigated here, where the resonance frequency is expected to shift when varying R and r^* for filter 1 and filter 2, respectively. See Figure 3.3 for definitions of R and r^*. Similar filter designs have been reported by Arafa et al. [17] and Takagi et al. [43], and have been used for inspiration for the two filter designs in this thesis. In literature, filter 1 is commonly denoted a *H0 cavity*, and filter 1 a *H1 cavity*. H0 and H1 will be used through the rest of this thesis for the different filter designs studied.

(a) Filter 1: H0 cavity　　　　　　　　(b) Filter 2: H1 cavity

Figure 3.3: The two kinds of filter designs investigated, consisting of cylindrical (air) holes with varying radii in a silicon slab.

Transmission spectra were computed in MEEP by exciting a gaussian pulse on the left side of the structure covering the frequency range of interest. The accumulated power

through a port on the right side was measured. To normalize the transmission a reference run was done first by exciting the same pulse and measuring the accumulated power through a strip silicon waveguide of the same length as the photonic crystal. A discussed in Section 2.1.3, only the TE-modes are of interest. Therefore, the gaussian pulse was set to have the electric field in the y-direction (in-plane, perpendicular to the waveguide). The simulation geometry with source, port and perfectly matched layers is shown in Figure 3.4 for a H0 filter. An example code with more explanation is given in Appendix B.

To get representative transmission spectra, it is necessary to let the simulation run for some time after the pulse is excited, since it takes time for the resonance to build up inside the cavity, and leak out to the output waveguide and through the port. Therefore, the output power is measured throughout the simulation, and compared to the peak value. When the output power is significantly lower than the peak value, the simulation is terminated. All 2D simulations were run until the output power was reduced to 10^{-5} times the peak value, ensuring that the remaining field power in the structure is very small. It should be noted, that a sharper resonance will need more time to leak out of the cavity, making simulations of high-Q resonances time consuming. Especially when performing 3D simulations, this might cause inexpediently long simulation times, so compromises might have to be made, ensuring both reasonable computation times and sufficiently accurate transmission spectra.
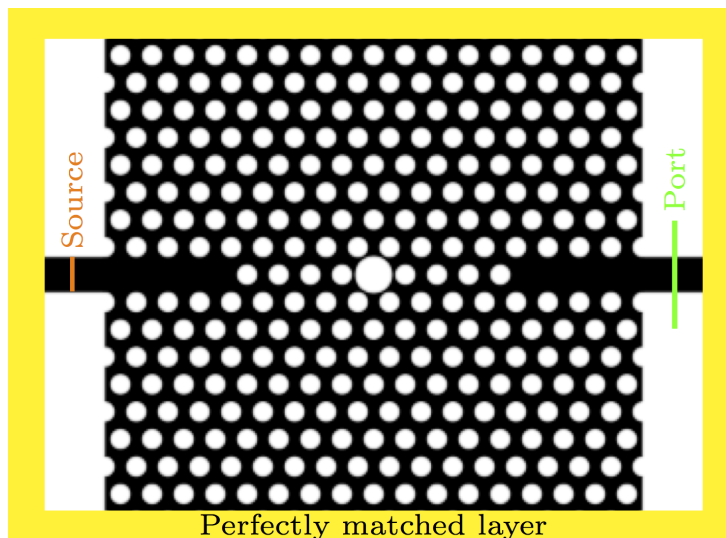

Figure 3.4: Simulation geometry for 2D simulations of a H0 filter. A pulse is excited at the source plane (orange), and the accumulated flux is measured through the port (green). Perfectly matched layers absorbing all incoming fields are applied to all outer boundaries.

3D simulations

Three-dimensional simulations of transmission filters turned out to be very time consuming when performed on a personal laptop. Therefore, only the H0 filter was simulated in three dimensions. The same geometry as for the 2D simulations shown in Figure 3.4 was used for 3D simulations. In addition, the silicon slab and air cylinders were assigned a thickness, and the underlying substrate and overlying air was specified. In addition, the source and port were specified as two-dimensional planes instead of lines. Also, PML's were applied to all outer boundaries of the three-dimensional "box". To avoid long computation times, the simulations were terminated when the output power was reduced to 10^{-3} times the peak value. In order to investigate the effect of functionalization, these simulations were carried out in an aqueous environment, meaning that the areas with air (cylinders and surrounding material) were substituted with material parameters of water. The same simulation geometry as for the waveguides was used (see Table 3.2).

Q-factors and mode profiles were obtained using the harminv plugin, by exciting the same pulse and the same position as used for the transmission computations.

3.2.5   Functionalization

Immobilization of binding agents on a surface, and the binding of relevant biomarkers to the binding agents, will be referred to as *functionalization* in the following. Functionalization is imitated by changing the refractive index. The biolayer thickness used in these simulations is set to 20 nm. The actual thickness of a biolayer containing the relevant biomarkers is difficult to predict, but 20 nm is a reasonable estimate, as reported values of protein layer thicknesses are around 15 nm [44]. Even if the estimate might be slightly too generous, it is still usable to compare different methods of functionalization, which is the main objective. The refractive index for the biolayers is set to 1.46, as is reported for a thin film of APTES [45], which is used for testing photonic biosensors in our research group. Functionalization was done in different ways: Applying a biolayer inside the cylinders, and applying a biolayer on parts of or the entire surface. A spectral shift of 0.1 nm is used as a critical limit for being able to detect with the current equipment in our lab. This number should not be emphasized too much, as other factors (Q-factor and the signal-to-noise ratio) are important in this context. Functionalization of the inside of the cylinders is considered much more laborious than functionalizing only the top surface, and it is therefore interesting to investigate whether functionalizing the top surface gives a sufficiently big resonance shift.

As one eventual objective is to fabricate a compact multiplexed device consisting of several filters placed close together, it is interesting to know how big an area of the surface needs to be functionalized in order to achieve sufficient shift. This is investigated by changing the RI of squares of different sizes centered at the cavity. Figure 3.5 illustrates a functionalized area of $4a \times 4a$.
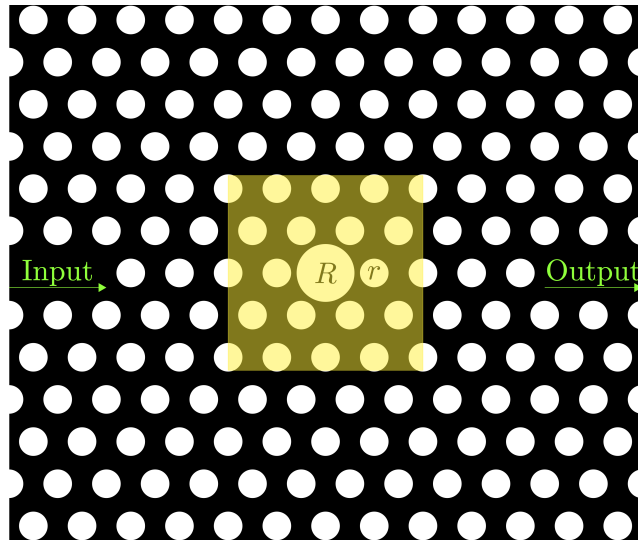

Figure 3.5: Functionalization of a $4a \times 4a$ square on the surface of a transmission filter.

3.3 Fabrication

The starting point for the fabrication process was 4 inch c-Si wafers (5 µm thickness) with 1000 nm thermally grown SiO_2, bought from University Wafer. Initially, the wafers were cut into smaller pieces of 15×15 mm with a Dynatex DX-III scribing and breaking tool. The process parameters presented in the following sections are based on the work done by Holmen [2] and Stein [3], in addition to further process optimization done by the author, which is presented in Chapter 4.

3.3.1 Silicon Deposition

a-Si was deposited with a PLasmaLab System 100-PECVD from Oxford Instruments, with silane (SiH_4) as silicon source. The process parameters are summarized in Table 3.3, and the process steps are presented in the following list:

- **Cleaning:** 2 min ultrasonic bath in acetone, followed by 2 min ultrasonic bath in ethanol. Rinsing with IPA and drying with an N_2 gun.

- **Chamber preconditioning:** A preconditioning step was performed by depositing silicon for 3 min on a dummy wafer.

- **Deposition:** Done for 170 s with the process paramaters listed in table 3.3.

Table 3.3: Process parameters for deposition of a-Si.

Parameter	Value
LF power	200 W
Pressure	500 mTorr
Table heater	300 °C
SiH_4	50 sccm
Ar	150 sccm
Deposition time	∼170 s

3.3.2 Electron Beam Lithography

The instrument used for patterning is an ELS-G100, a 100 kW electron beam lithography system by STS-Elionix. It has an electron beam size down to 1.8 nm and is capable of generating patterns with line widths down to 7 nm [33].

Layout Design and Preparation

The desired patterns were designed in CleWin4, a layout editor by WieWeb Software [46]. The layout is then processed in Beamer, a software from GenISys GmbH [47]. Firstly, the layout is corrected for overlapping features, to avoid double exposure of those areas. Next, proximity error corrections and bulk and sleeve splitting of the pattern is done, as described below. Finally, the structure is divided into write fields of desired size (typically in the order of $1\,\mathrm{mm} \times 1\mathrm{mm}$). During exposure, one write field is exposed at a time, and the stage moves to center the next write field. During this process, inaccuracies in the stage movement and slightly different properties (angle, focus, astigmatism) of the beam at different positions in a write field can result in small alignment errors at the interfaces between write fields. To make these less prominent, *multi-pass* exposure is done meaning the system is set up to expose twice with half the desired dose each time, with the write fields shifted. All this data is then exported to a library of files that are imported into WecaS, a software by STS-Elionix, where the processed pattern is aligned to the sample. The beam is adjusted to have the desired current, and to be in focus and without astigmatism.

As a last step before exposure, *field correction* is performed. This is done to reduce alignment errors between the stage and the electron beam, which is crucial for reducing the mismatch between neighboring write fields, called *stitching errors*. Field correction is done automatically by the EBL system by scanning the beam across a known feature, then moving the stage approximately 1/3 of the write field size and scanning again, to get information on where the beam is relative to how much the stage has moved. This is repeated nine times in different directions. This entire process is repeated until the mismatch between the beam and the stage during stage movement is within a tolerance value of $20\,\mathrm{nm}$.

Proximity Error Corrections

Due to scattering of the electron beam in the resist and the substrate, areas outside the electron beam will also be exposed. Therefore, bulk areas will tend to get more exposure than edge areas, as they will experience electron scattering from surrounding areas, called the *proximity effect*. To compensate for this effect, different radiation doses have to be used for different areas on the sample. The electron scattering in the resist and substrate are calculated with a Monte Carlo simulation done with the software package Tracer from GenISys GmbH [48]. Based on the results from the Monte Carlo simulation, the software

Beamer is used to divide the pattern into smaller areas and assign appropriate exposure doses to each area.

Bulk and Sleeve Exposure

Different areas of a complex structure might require different degrees of accuracy during exposure. During exposure of big areas at a low current, a clever trick can be to divide the structure into one bulk part, containing the larger non-critical parts of a structure such as the interior of a waveguide, and one sleeve part, containing critical features such as waveguide edges and photonic crystals. Then the bulk can be exposed at a higher current, which is less time consuming, allowing for accurate patterning of large areas within a reasonable time frame.

Process Parameters

The process steps with relevant parameters for the EBL exposure are presented in the following list:

- **Dicing:** The wafer was diced in to smaller pieces (15x15 cm) with a scribing/breaking tool.

- **Cleaning:** Ultrasonic bath in acetone for two minutes, and ultrasonic bath in ethanol for two minutes, followed by washing with IPA, and blow-drying with nitrogen gas.

- **Spin coating:** Done for $60\,\mathrm{s}$ at $3300\,\mathrm{rpm}$, with an acceleration of $1000\,\mathrm{rpm/s}$. This should give a resist thickness of $475\,\mathrm{nm}$.

- **Soft bake:** $150\,°\mathrm{C}$ for $1\,\mathrm{min}$.

- **Exposure:** Exposure is done with a beam current of $1\,\mathrm{nA}$ ($100\,\mathrm{pA}$ and $5\,\mathrm{nA}$ when doing bulk and sleeve). The exposure dose used was $350\,\mathrm{\mu C/cm^2}$. The pattern was divided into write fields of size $500\,\mathrm{\mu m} \times 500\,\mathrm{\mu m}$. Exposure was carried out twice with half the required exposure dose, with shifted write fields (multi-pass exposure).

- **Development**: Exposed samples were developed in a AR 600-546 solution for $1\,\mathrm{min}$, then dipped in IPA for less than a second to stop the development, then rinsed in IPA for $30\,\mathrm{s}$.

3.3.3 Plasma Cleaning:

Between resist development and etching, a plasma clean was performed. The reason for this is that there often are small pieces of resist left on the sample, working as masks on places where there should not be resist left. Plasma cleaning was done with a Diener Electronics, model Femto, with an oxygen plasma. The process parameters are listed in Table 3.4.

Table 3.4: Process parameters for plasma cleaning.

Parameter	Value
O_2 gas flow	100 sccm
Generator frequency	20 kHz
Time	60 s

3.3.4 Etching

Silicon etching was done in a PlasmaLab System 100 ICP-RIE 180 by Oxford Instruments. Prior to etching, a 3 min preconditioning step was performed by etching a dummy silicon wafer, if the previous etching had been done with a different etching chemistry. The etching chemistry used was a mixture of CHF_3 and SF_6. Table 3.5 summarizes the parameters used in the etching process.

Table 3.5: Process parameters for silicon etching.

Parameter	Value
SF_6	7.5 sccm
CHF_3	50 sccm
Pressure	15 mTorr
CCP Power	40 W
ICP Power	600 W
Temperature	20 °C
Etch time	$\sim$45 s

3.3.5   Sample Overview

Figure 3.6 illustrates the design of the samples with conventional tapered silicon waveguides used for incoupling. The real dimensions are presented in Table 3.6. Several PhC or waveguide structures were fabricated on each sample, with a spacing of $30\,\mu$m between each structure, typically 15-20 in total. The entire collection of structures was then fabricated twice on each sample, to have a backup in case of defects occurring in the structure.
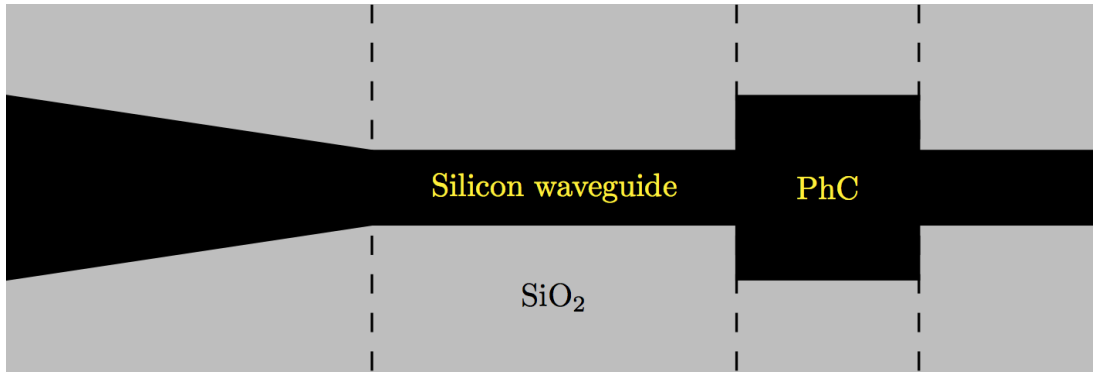

Figure 3.6: Schematic of the sample design, with tapered silicon waveguides for light incoupling. The sizes are not to scale, see Table 3.6 for real dimensions.

3.3.6   Initial fabrications

The first fabrication iterations were carried out using the recipe presented above, to verify that the process parameters were correct. The actual dimensions in fabricated samples were studied with SEM, and compared to intended dimensions in the mask design, which were adjusted after every iteration to approach the desired dimensions. Whether the etching process parameters yielded etching through the entire silicon layer was investigated with SEM. Plain silicon strip waveguides were fabricated in addition to PhC waveguides, to compare transmission spectra. Exposures both with and without bulk and sleeve were done, to investigate if bulk and sleeve gave better results than conventional single-current exposure. If proven so, bulk and sleeve would be utilized eventually, after first optimizing the structures with less time-consuming, conventional exposure.

3.3.7   Inverted-taper waveguides

Initial samples were fabricated with a tapered silicon waveguide for coupling of light from the fiber, as described in Section 3.3.5. Due to the small geometric overlap, and large

mismatch in mode sizes and refractive indices between the fiber and the SOI waveguide, high coupling losses become a problem. The procedure and experimental setup for coupling light into the sample is described in Section 3.4.1. Therefore, an alternative design, using an inverted taper embedded in a polymer cladding was tested. This has been reported to give significantly lower losses than when coupling directly into an SOI waveguide [24].

Figure 3.7 illustrates the sample design with an inverted taper silicon waveguide embedded in a polymer cladding, which consists of the negative electron resist SU-8. The additional fabrication steps needed are summarized in the following list:

- **Silicon patterning:** The silicon patterning is done in the same way as described in Section 3.3.2, with one small change: To be able to align the polymer cladding to the inverted silicon tapers, alignment marks were also patterned and etched into the sample. The EBL system has a tool for aligning a new exposure to existing alignment marks, using the SEM functionality of the EBL to find the exact position of the marks.

- **Cleaning:** If done immediately after removal of the CSAR-62 resist, no extra cleaning was done before spin coating with SU-8 from MicroChem. If not done immediately after resist stripping, cleaning with IPA and blow-drying with N_2 was done.

- **Spin coating:** At 3000 rpm for 36 s, with an acceleration of 500 rpm/s. This should give a thickness of around 2 µm.

- **Soft bake:** On a hotplate at 95 °C for 1 minute.

- **Exposure:** With a 500 pA current, and a dose of 30 µC/cm^2.

- **Post exposure bake:** On a hotplate at 95 °C for 3 min.

- **Development:** In SU-8 developer provided by MicroChem for 20 s, then another 20 s in another beaker containing SU-8 developer, and finally 30 s in IPA.

3.3.8   Transmission filters

After having optimized the fabrication procedure to yield samples of good and consistent quality, a large number of transmission filters were made, combining different lattice constants of the PhC structure and different values of r, r^* and R (bulk radius, radius of the central cavity in the H0 filter and radius of holes surrounding the cavity in the H1
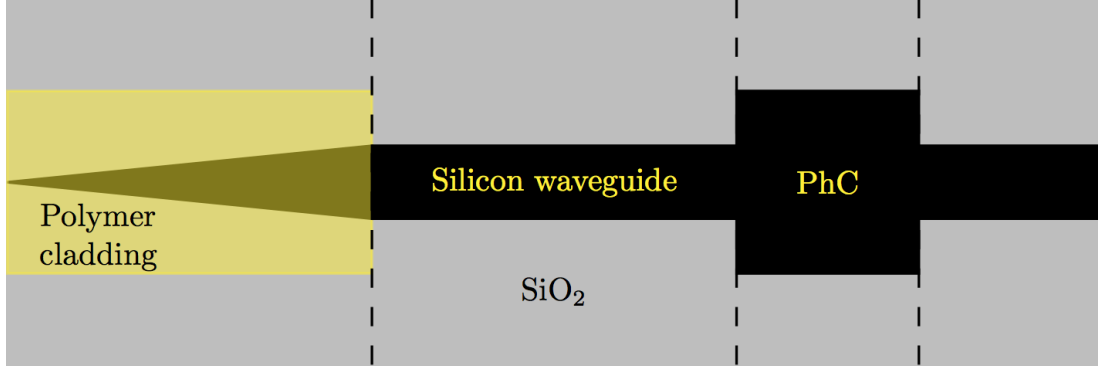
Figure 3.7: Schematic of the sample design of an inverted silicon taper embedded in a polymer cladding. The sizes are not to scale, see Table 3.6 for real dimensions.

Table 3.6: Dimensions of the fabricated samples.

Component	Length [µm]	Width [µm]
Tapered waveguide	600	5-0.5
Inverted taper waveguide	600	0.07-0.5
Input waveguide	1000	0.5
Output Waveguide	1000	0.5

filter, respectively). The reason for varying all these parameters, and not only stick to the parameters used for the simulations, is that the physical material parameters (refractive index) might deviate somewhat from the values used in simulations, giving different transmission properties of the devices. Table 3.7 summarizes the combinations of parameters in fabricated transmission filters. Initially, the H0 filter was fabricated with $n_c = 3$ and the H1 filter with $n_c = 2$. The reason for choosing these values for n_c, and not higher values of n_c, is that they give broader resonance peaks, which are expected to be easier to identify during optical characterization. If proven to function, n_c could be increased and the narrower peaks should be located at approximately the same wavelengths.

Table 3.7: Different values of parameters combined in the fabricated transmission filters.

Parameter	Values
a	390 nm, 410 nm, 430 nm
r	$0.27a$, $0.30a$
R	$0.54a$, $0.57a$
r^*	$0.16a$, $0.18a$

3.4 Characterization

3.4.1 Optical Characterization

Figure 3.8 illustrates the setup used for optical characterization of the samples. The components' manufacturer and model are summarized in table 3.8. Two different methods of characterization were used: Recording of the IR laser's propagation through the device with an IR-camera, and measurement of the transmission through the device. Accurate alignment is crucial to achieve light coupling. The samples were aligned to the input and output fibers with the help of the microscope.

Investigation with IR-camera

Due to scattering losses at imperfections in the waveguide, it is possible to see the light as it propagates in a strip waveguide with the IR-camera. This is useful when aligning the sample, to achieve best possible light coupling. When characterizing the transmission filters, it was difficult to align the output fiber, as there is no transmission for most wavelengths (except for the resonance wavelength). Therefore, the IR camera was used to find the resonance wavelengths, where the light was transmitted through the filter. At these wavelengths, the output fiber was aligned.

Transmission Measurements

After aligning the samples, the laser was tuned from 1480 to 1620 nm, and the transmission spectra were recorded. Further alignment was done by small adjustments of the fibers to find the maximum amplitude of the transmitted light.

3.4.2 Scanning Electron Microscopy

The samples were inspected with scanning electron microscopy (SEM). The instrument used is a FEI Apreo SEM. Images were taken with an acceleration voltage of 5 kV. SEM imaging was useful to detect defects and inspect the quality of the fabricated devices. It was also used to measure actual sizes of the patterned features, which might be different than the sizes in the mask design due to electron scattering during EBL, and anisotropy during etching. Measurements of real sizes from the SEM images were done with an edge detection plug-in implementing the Canny edge detection algorithm [49] in the image software ImageJ [50].
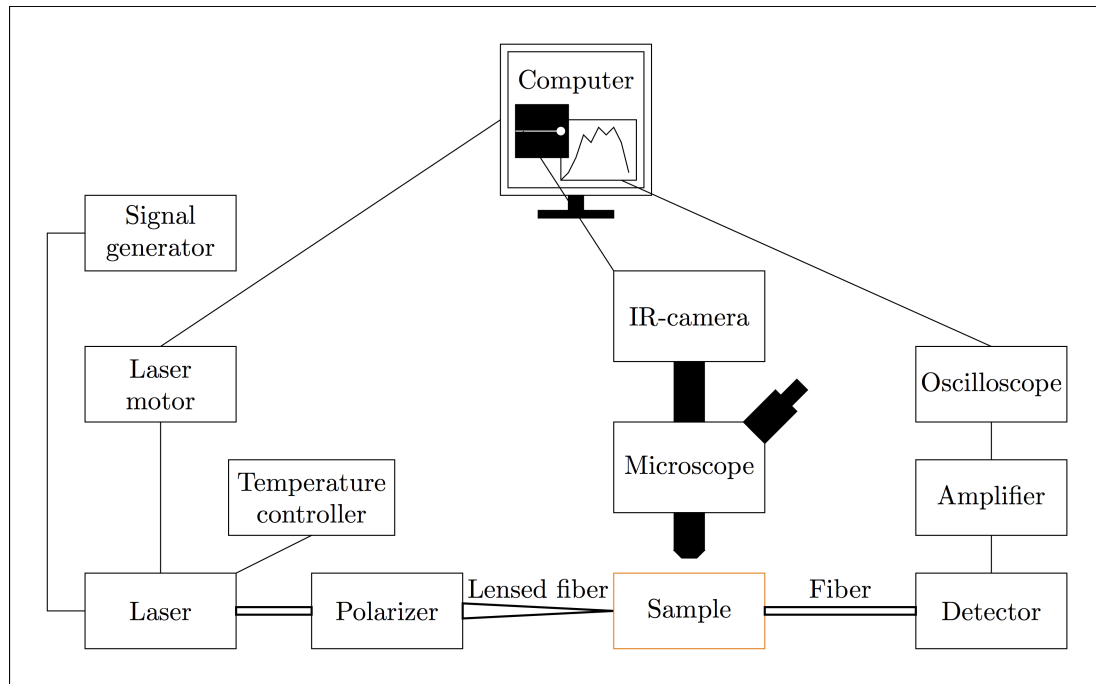
Figure 3.8: Setup for performing transmission measurements through samples and IR imaging of the sample surfaces.

Table 3.8: Manufacturer and model for the components used for optical characterization of the samples.

Component	Manufacturer	Model
Signal generator	Newport	505
Temperature controller	Newport	325
Laser motor	Thorlabs	TDC001
Laser	Thorlabs	TLK-L1550M
Polarizer	Thorlabs	-
Lensed fiber	Nanonics Imaging	-
Sample stage	Elliot	MDE881-60
Microscope	Leitz Wetzlar	-
Objectives	Olympus	LMPlan 10x IR, SLMPlan 20x
IR camera	Hamamatsu	C14041
Detector	-	InGaAs PIN diode
Amplifier	Thorlabs	PDA200C
Oscilloscope (digital)	National Instruments	Labview 2015

Chapter 4

Results and Discussion

In this chapter, results from the simulation and fabrication processes are presented. As the early results form a basis for the following experiments, results are discussed consecutively throughout the chapter. As a starting point, very basic simulations of material parameters and two-dimensional PhC band structures were performed. These formed a basis for subsequent simulations of PhC waveguides and transmission filters in two and three dimensions. The simulation results are used to motivate the choice of parameters in the fabrication process. Several process parameters were investigated and optimized, before components like PhC waveguides and transmission filters were fabricated and optically tested.

4.1   Simulations

All the simulations in this chapter are based on a PhC consisting of silicon with a hexagonal pattern of air cylinders.

4.1.1   Design Requirements

As a prerequisite for understanding the choice of parameters throughout the simulations, the requirements and guidelines for a good PhC waveguide stated in the theory chapter, section 2.1.3, are repeated here. The following are considered to be *requirements* for having a functioning waveguide:

- There must exist guided modes (modes within the band gap of the bulk PhC) covering the frequency length of interest.

- These modes must also be index guided (lie below the light line).

- There should be no leaky modes (inside the light cone) at the same frequencies.

In addition, to optimize the waveguide performance, the following guidelines should also be considered:

- A larger bandgap will better confine guided modes.

- The modes that lie near the middle of the band gap are better confined.

- A larger dispersion (larger slope) of the guided modes' bands below the light line will result in a broader transmission spectrum.

All of the aspects mentioned above cannot necessarily be optimized simultaneously. Compromises might have to be made so the fundamental requirements are met, and fulfillment of the additional guidelines should be striven for.

4.1.2   Two Dimensional Approximation of a PhC Slab

Since 3D simulations are expensive in terms of time and computational capacity, it is necessary to approximate 3D PhC slab structures with a 2D model. In a 220 nm thick silicon slab, as used in this project, the effective RI of the propagating modes is different than for bulk silicon. The *effective refractive index*, n_{eff}, was therefore simulated, and found to be $n_{eff} = 2.846$, corresponding to an $\varepsilon_{eff} = n_{eff}^2 = 8.10$, which is close to earlier reported values for similar structures [51]. This value is used in the following 2D simulations.

Such an approximation of the effective refractive index is good when the RI contrast between the layers in the structure is small. If the RI contrast is big, as it is considered to be for the SOI structure used in this project, the effective refractive index will change significantly with varying wavelength. However, within the relatively narrow wavelength spectrum investigated in this project (1.48 to 1.62 µm), the RI variation is small (it has been reported to vary with around 7 % for a wavelength range of 0.1 µm centered at 1.55 µm [52]). Therefore, this approximation is considered reasonable. In any case, even if it is not completely accurate, it is good enough for approximating 3D structures with a 2D model for initial tuning of parameters before performing 3D simulations, which greatly decreases the requirement for computational power and/or simulation time.

4.1.3   Photonic Band Gap

As mentioned in the previous section, it is beneficial to have as large a bandgap as possible. The band structure was computed for a 2D PhC with MPB for different values of r/a, and the resulting relation between the band gap size (gap-midgap-ratio) as a function of r/a is given in Figure 4.1.
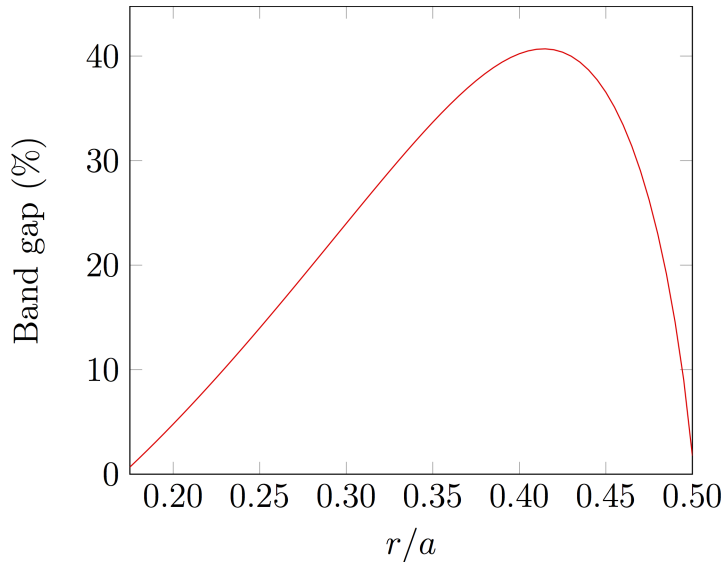

Figure 4.1: Two dimensional PhC band gap size (expressed in terms of the band-midgap-ratio) as function of the hole radius divided by the lattice constant (r/a-ratio). The PhC is a silicon slab with a hexagonal pattern of air cylinders.

The band gap maximum occurs at $r/a = 0.415$, where the gap-midgap-ratio is just above 40 %. Choosing the r/a-ratio with the lagrest band gap might be tempting, but as discussed in Section 2.1.3, there are several aspects regarding the dispersion relations of the modes needing to be considered to be able to choose a suitable r/a-ratio. There are some remarks to be made when considering the band gap as function of r/a-ratio isolated. Firstly, the slope of the band gap curve is steeper on the right hand side (with increasing r/a) of the maximum. Therefore, choosing a r/a-value above the maximum would make the device more sensitive to inaccuracies during fabrication. Secondly, making the hole radius larger means that the thickness of silicon between the air cylinders become smaller, which might cause additional challenges during fabrication. It is therefore reasonable to aim for an r/a-ratio below the maximum. These considerations will be combined with the findings regarding the dispersion characteristics in the following section, when deciding for an r/a-ratio to use for the transmission filters.

4.1.4   Linear Defect Waveguide

The band structures computed with MPB for a two dimensional PhC for different values of r/a is given in Figure 4.2. The band gap clearly gets bigger for increasing r/a-ratio, as was expected from the previous section. What is more important however, is the dispersion of the guided modes. Modes lying within the light cone will leak into the substrate, and frequencies for which such leaky modes exist will experience losses when propagating in the waveguide.

The waveguide should be able to guide light in the wavelength range 1.48 μm to 1.62 μm, which is the range of the laser used in our setup for optical characterization. At least, a major part of this range should be covered. For a wavelength range of this size to be guided, it is necessary to have a mode with enough slope (dispersion) outside the light cone, for which there are no other modes within the light cone at the same frequencies. If the band is flat outside the light cone, it means that only a very narrow spectrum of wavelengths can be guided. This can in some applications be useful (for example where *slow light* is desired [53]), but obviously not for this application, as we need to cover the desired range. This requirement is best satisfied with decreasing r/a-ratio, where the lowest gap-guided mode has a slope outside the light cone. For $r/a = 0.3$, this slope is big enough to cover a wavelength range from 1.51 μm to 1.59 μm, which is considered sufficient. A smaller r/a would also probably have been a reasonable choice, but an argument against much smaller cylinders is that they become more difficult to fabricate. $r/a = 0.3$ is therefore chosen as the cylinder radius for further simulations. During fabrication, radii of $0.27a$ and $0.3a$ are tested.

The wavelength range of the lowest gap-guided mode outside the light cone is visualized in Figure 4.3(a). This range will be referred to as the *operating region* from now on. By centering the operating region around $\lambda = 1.55$ μm, the corresponding lattice constant of a physical structure becomes $a = 407$ nm. As a reminder, the relationship between the lattice constant, dimensionless frequency (ω_{dl}) and physical wavelength is given by:

$$\omega_{dl} = \frac{a\omega}{2\pi c}, \qquad \lambda = \frac{a}{\omega_{dl}}. \tag{4.1}$$

The band structures and simulated transmission spectra from MPB and MEEP are presented in terms of dimensionless frequency, while optically measured transmission spectra later on are presented in terms of physical wavelength. All the following transmission spectra are obtained for structures with $a = 407$ nm.

In Figure 4.3 an excerpt of the band diagram together with a 3D transmission spectrum of a waveguide with $r/a = 0.3$ are displayed. The first thing to comment is that the
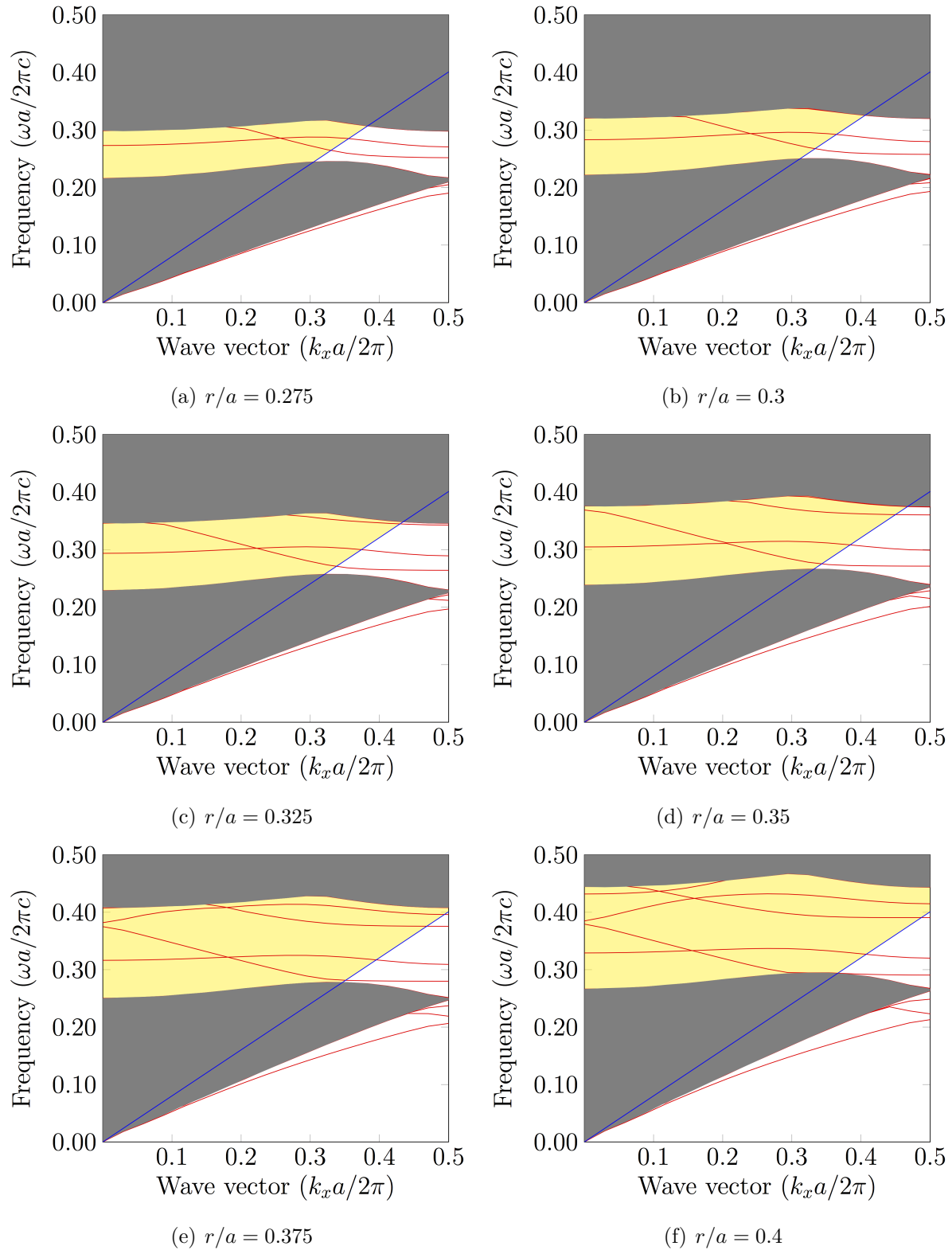
(a) $r/a = 0.275$

(b) $r/a = 0.3$

(c) $r/a = 0.325$

(d) $r/a = 0.35$

(e) $r/a = 0.375$

(f) $r/a = 0.4$

Figure 4.2: Band structures for 2D PhC waveguides consisting of a missing row of cylinders, for varying values of r/a.

onset for high transmission (at 0.265 in units of dimensionless frequency) is not located at the lower border of the operating region (at 0.258), as would be expected. The main reason for this is suspected to be that the band diagram is computed using a 2D model, while the transmission spectrum is computed with a 3D model, revealing the inaccuracy of the effective refractive index approximation. In addition, the two simulations are performed in different software (MPB and MEEP), using different computational methods (frequency-domain and time-domain), which could cause some deviation from one to the other. Nonetheless, the qualitative behaviors of the two different simulations are comparable and together they reveal some key properties of a linear defect waveguide. Below the band gap, there is a continuum of modes, all being leaky into the photonic crystal, which explains why there is poor transmission for the lowest frequencies. At the bottom of the band gap, there are no modes present, resulting in zero transmission for a small frequency range. Next, with increased frequency, the transmission increases abruptly where the lowest-lying defect band is positioned. From this point and throughout the band gap the transmission is maintained high, with a slight dip as the guided modes extend into the light cone causing some leakage. This effect is expected to be more prominent for a longer PhC waveguide (in this simulation, the number of periods in the waveguide direction is 17) [2]. At the upper edge of the band gap, the transmission is drastically reduced, as the radiation again can propagate into the photonic crystal, and is no longer confined in the waveguide.

The PhC structures used for simulations and fabrication of transmission filters in the next sections are of similar dimensions as the waveguide simulated here, with 17 periods in the direction of propagation. Since the transmission is high for a wide range of frequencies, this waveguide is believed to function well in combination with a transmission filter with resonance frequency within the high-transmission range.

This waveguide structure could certainly be optimized further. By adjusting the size of the cylinders adjacent to the waveguide, changing the width of the waveguide, or inserting smaller cylinders along the waveguide, one could tune the band diagram to have more dispersion, and to have an operating region closer to the band gap center [54],[55],[56]. As the main objective of this project was to simulate and fabricate a *functioning* PhC transmission filter, further tuning of parameters was not carried out, as the simple linear defect waveguide turned out to be sufficiently good for this purpose.
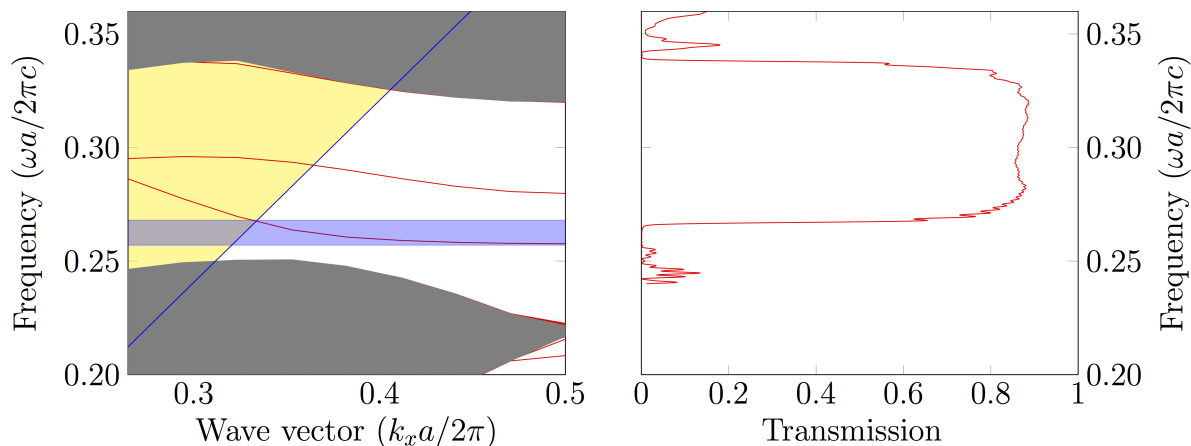
(a) Excerpt of the band diagram for a linear defect waveguide with $r/a = 0.3$. The blue shaded region indicates the operating region.

(b) Normalized transmission from a 3D simulation done with MEEP of a linear defect waveguide, with $r/a = 0.3$.

Figure 4.3: Excerpt of the band diagram (a) and a transmission spectrum (b) of a linear defect waveguide.

4.1.5 Transmission Filter

One of the requirements for the transmission filters was that the resonance frequency could be shifted by simple geometrical adjustments. This would make it possible to combine several similar filters into a multiplexed filter. Figure 4.4 shows how the resonance frequency is shifted by adjusting the radius of the central cavity (R) for the H0 filter, and the radius of the cylinders surrounding the cavity (r^*) for the H1 filter, confirming that both these filters could be suitable for use in a multiplexed device. This is also reported by Arafa et al. [17], where a multiplexed resonator based on a H0 cavity similar to the one studied here is simulated.

All the transmission spectra in this section are normalized by dividing the transmitted flux of the transmission filter by the transmitted flux of a strip waveguide. More details on how these simulations are done can be found in the Appendix.

It can clearly be seen that the Q-factors (the "sharpness" of the resonance peaks) are higher for the H1 filter than for the H0 filter. This behavior deserves some explanation, for which the mode profiles of the two different resonators are helpful. These are presented in Figure 4.5. The resonant mode in the H0 filter extends significantly more into the photonic crystal and throughout the waveguide than the resonant mode in the H1 filter does. The mode profiles are different: In the H0 filter, the resonant mode has a nodal

plane in the center (a dipole mode), which is not the case for the H1 mode. Since the filters are of different geometry, it is not straightforward to relate the Q-factors to the number of poles, but it is however expected that a mode without any nodal planes generally is better confined than a dipole mode in photonic crystal cavities [57],[58], which is in agreement with the findings presented here. As reported by Arafa et al. [17], it should be possible to obtain a mode without a nodal plane in a H0 filter by increasing R to a size where the remaining thickness of silicon between the central cavity and surrounding holes becomes very small, and probably difficult to fabricate properly. Further research to obtain such a mode for the H0 filter is therefore excluded. As discussed in Section 2.1.3, the resonant modes may come in doubly degenerate pairs (with a 90° rotation relative to each other), with slightly different resonance frequencies. Such peak splitting is not accounted for in the simulations, as the harminv plugin selects the "best" mode and calculates the quality factor for that exact mode. As will be discussed in Section 4.3.2, peak splitting may occur in a real transmission filter.

By increasing the number of cylinders (denoted as n_c) along the waveguide on each side of the cavities, the Q-factor is significantly increased, while the signal of the transmitted strength is slightly reduced. This behavior is shown in Figure 4.6, where transmission spectra for a H1 filter with two and three cylinders on each side of the cavity are compared. The explanation for this is quite simple: The larger number of cylinders on each side of the
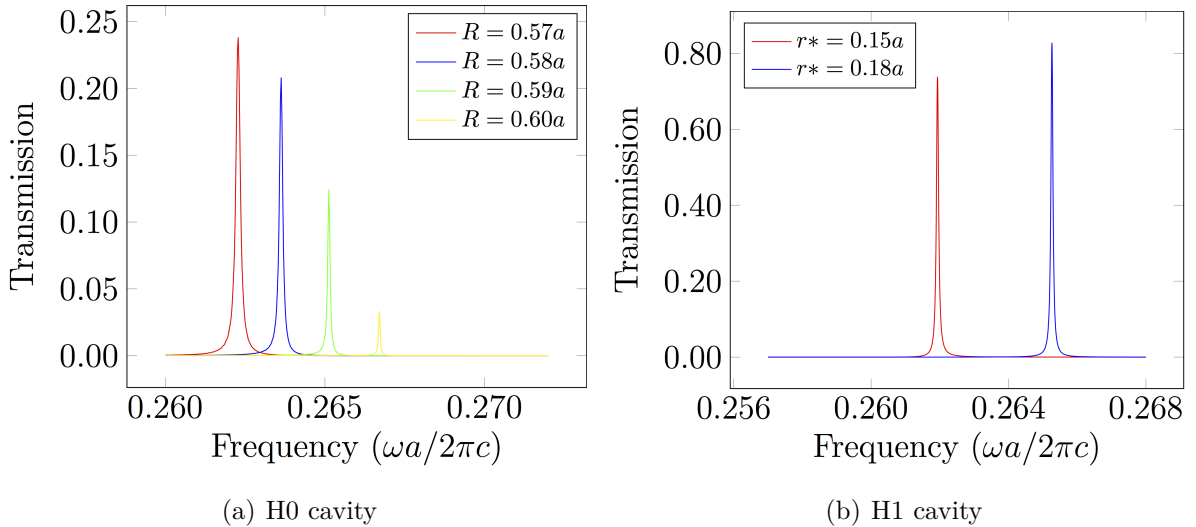

(a) H0 cavity

(b) H1 cavity

Figure 4.4: Transmission spectra for H0 and H1 filters with varying values of R and r^* from a 2D simulation with MEEP, showing that the resonance frequency can be tuned by simple geometrical adjustments. The simulation geometry is shown in Figure 3.3.

cavity, the less field power will couple in to and out of the cavity, as discussed in Section 2.1.3. The Q-factors for the different filters simulated in two dimensions are presented in Table 4.1, and are close to earlier reported values: The Q-factor of 57325 for the H1 filter with $n_c = 3$ and $r^* = 0.18a$ is close to the Q-factor (62000) reported by Takagi et al. [43]. For the H0 filter, the Q-factor found here is within the range of the Q-factor values (700-3820) reported by Wang et al. [43], for modes both with and without nodal planes in a similar geometry.

Comparing H0 and H1 filters it is clear that the H1 filter has the best performance, both in terms of Q-factor and strength of the transmitted signal.

3D Simulations

It was further attempted to perform three dimensional simulations for both filters, but as those simulations turned out to be very time consuming, reasonable results were obtained for the H0 filter only. However, as presented in Section 4.3.2, both filters were fabricated and proved to work in a real SOI slab. A transmission spectrum from a 3D simulation of the H0 filter is presented in Section 4.1.6, where the effect of adding a biolayer to the filter was investigated.

The Q-factor for the H0 filter, with $R = 0.6a$ was found to be 932. Comparing with the 2D simulations, the resonance peak is broader, and the transmitted signal is of similar strength, and it is believed to be good enough for investigating the effects of
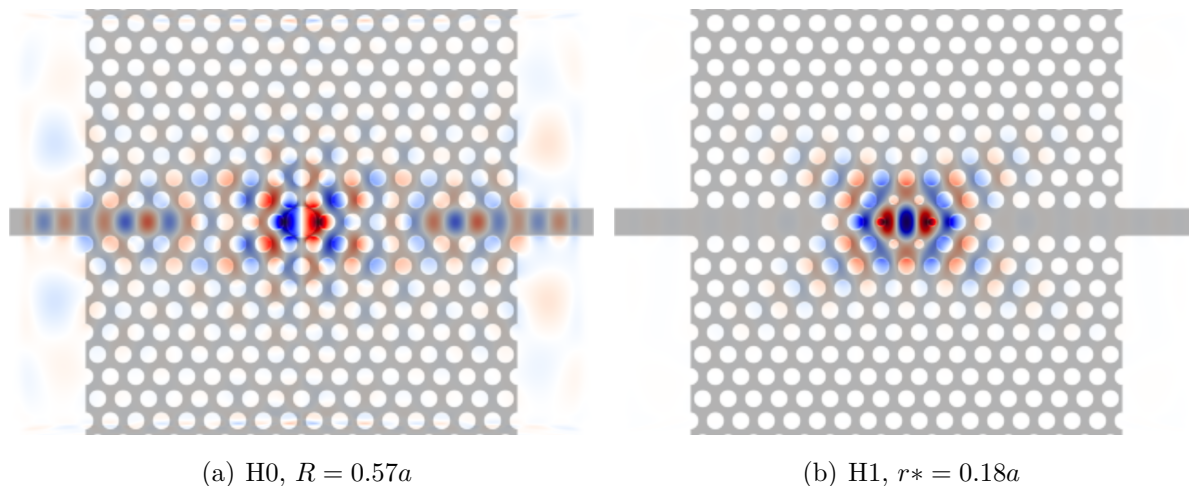

(a) H0, $R = 0.57a$ (b) H1, $r* = 0.18a$

Figure 4.5: Mode profiles for resonant modes in the two filters, from a 2D simulation done with MEEP.

(a) Two cylinders on each side of cavity

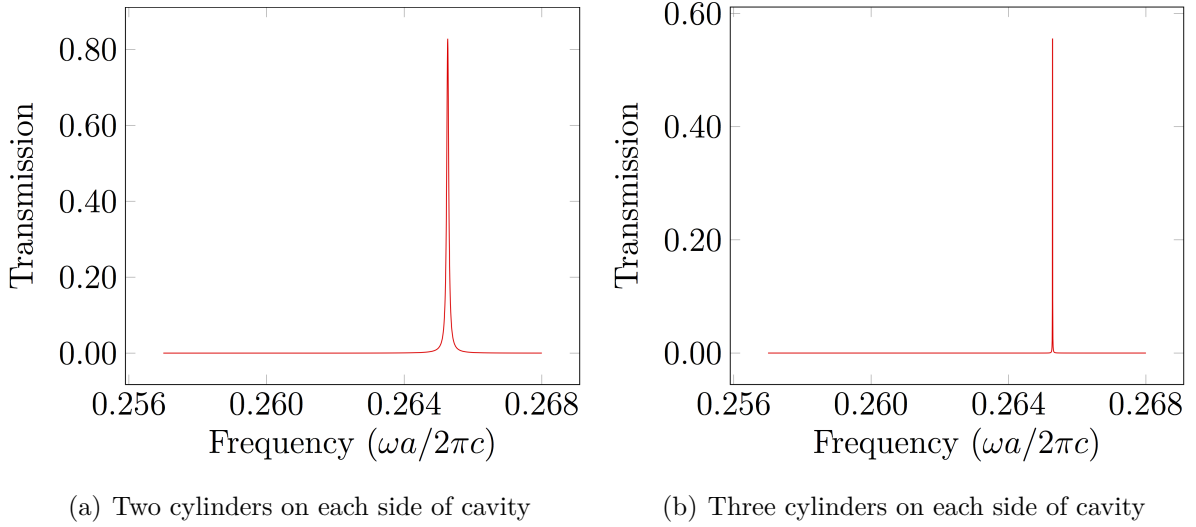(b) Three cylinders on each side of cavity

Figure 4.6: Transmission spectra computed in two dimensions for the H1 filter with $r^* = 0.18a$, with two ($n_c = 2$) and three ($n_c = 3$) cylinders on each side.

functionalization, which is done in the following section. It is expected that a successful 3D simulation of the H1 filter would give a resonance peak with a significantly higher Q-factor, based on the values obtained in the 2D simulations.

Table 4.1: Q-factors for different filter designs, from 2D simulations done with MEEP.

Filter type	Q-factor
H0, $R = 0.57a$, $n_c = 4$	1635
H0 (3D) $R = 0.6a$, $n_c = 4$	932
H1 $r* = 0.18a$, $n_c = 2$	3874
H1 $r * 0.18a$, $n_c = 3$	57325

4.1.6   Functionalization

For the transmission filters to function as biosensors, it is necessary that a shift of the resonance frequency is induced by applying a biolayer to the device. This can be done in different ways: A biolayer can be applied inside the cylinders, or it can be applied only on top of the silicon surface. The former is more complicated, as it requires functionalization on the inside of the tiny cylinders with molecules that bind to the target biomarkers. Covering only the silicon surface (or parts of it) on the other hand would be a much easier

process. The impact of both types of functionalization is therefore compared, for a H0 filter, with $R = 0.6a$. The results, in terms of how much the resonance peaks shift as a result of different functionalization is presented in table 4.2. The reference transmission peak (without biolayer) is obtained from a simulation with water inside the cylinders and on top of the SOI slab, since the biosensor is supposed to operate in aqueous conditions.

Table 4.2: Resonance frequencies and corresponding wavelengths for different methods of functionalization, calculated from 3D simulations of the H0 filter with $R = 0.6a$ and $n_c = 4$.

Type of biolayer	Resonant frequency $[\omega a/2\pi c]$	Wavelength [nm]	Shift [nm]
No biolayer	0.255580	1592.53	0.00
Entire surface	0.255279	1594.33	1.80
$3a \times 3a$ square on the surface	0.255403	1593.55	1.02
$4a \times 4a$ square on the surface	0.255377	1593.72	1.19
Inside central cavity	0.255574	1592.49	-0.04
Inside central cavity and six nearest neighbors	0.255650	1592.02	-0.51

Figure 4.7 shows the transmission spectra for the H0 filter with $R = 0.6a$ with and without a biolayer on top (covering the entire surface) of the SOI slab, from a 3D simulation with MEEP. The findings summarized in Table 4.2 show that the resonance frequency is shifted when applying a biolayer in different ways. The largest shift (1.80 nm) occurs when covering the entire surface. This shift is slightly reduced when reducing the area covered. The reason for covering a smaller area instead of the entire surface is the idea of combining several filters into a compact, multiplexed device, where smaller areas of the sample (for each filter) would need to be functionalized differently, to enable detection of several biomarkers simultaneously. The shifts for a $3a \times 3a$ (1.02 nm) and $4a \times 4a$ (1.19 nm) are of such a magnitude that they should be possible to detect.

Interestingly, applying a biolayer inside the cylinders resulted in a blueshift in the resonance frequency. This contradicts the results by Lee and Fauchet [6]. Applying a biolayer on top gave a redshift, which is as expected [6],[59]. The reason for the blueshift is not obvious, but one possible explanation could be that when applying a biolayer inside the cylinders, the periodicity of the PhC is altered, in that a third dielectric constant is introduced in the periodic dielectric function. This could cause the entire band structure to shift towards higher frequencies, opposing the expected redshift.
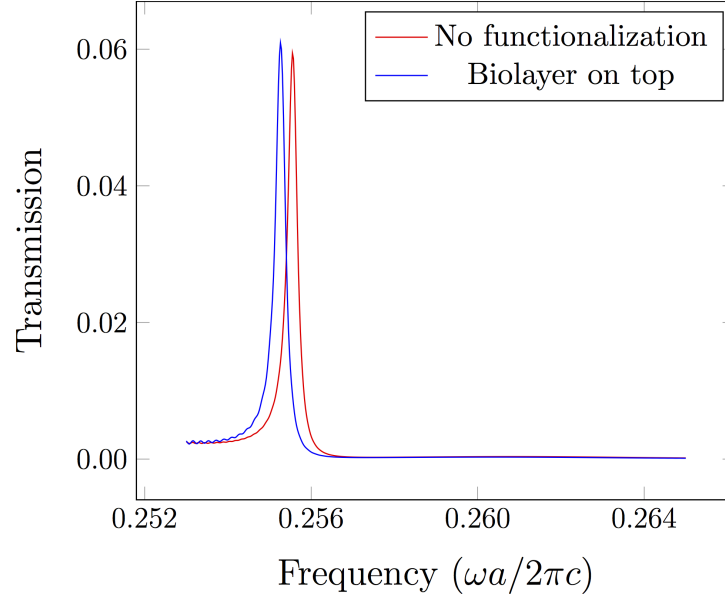
Figure 4.7: Transmission spectra for The H0 filter ($R = 0.6a$) with and without a biolayer on top of the SOI slab, from a 3D simulation with MEEP.

4.2   Fabrication

4.2.1   Initial Fabrication Results

The initial fabrication iterations were used to check if the process parameters yielded samples of good quality. SEM images of the cross-section of an intentionally broken sample revealed that etching through the entire silicon layer was achieved with an etching time of 45 s. The quality of the initial samples was generally good, with uniform holes and smooth waveguide sidewalls. However, there was an issue with cracks occurring in the resist that was transferred to the silicon during etching, as is described in the following.

Resist Cracking

During initial fabrication cycles, problems with resist cracking of CSAR-62 after exposure and development were encountered, see Figure 4.8, where both an optical microscopy image of the resist and an SEM image of the etched silicon are shown. As it interrupts the photonic crystal structure, bends the entire structure (as can be seen in Figure 4.8(b)), and generally is an unpredictable source of error, resist cracking should be avoided. The reason for cracking was not obvious, but hypotheses of three possible reasons were investigated. Firstly, it was suspected that in the baking step (between spin-coating and exposure) the

temperature was too low and time too short. The effect of increasing the temperature and time was investigated. Secondly, it was observed that the cracks were initiated at sharp features, for example corners of a waveguide. Therefore, attempts of rounding the edges in the mask design were done. Secondly, it was evident that the larger the distance between two neighboring waveguides (up to some limit), the more cracks were formed.
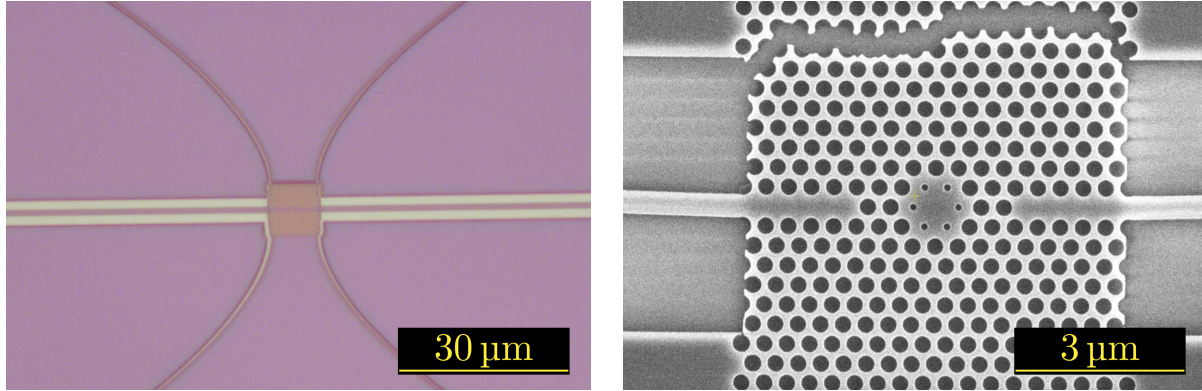
(a) Optical microscopy image developed CSAR-62 resist, with cracking.

(b) Optical microscopy image developed CSAR-62 resist, with cracking.

Figure 4.8: Optical microscopy (a) and SEM (b) images of cracking in developed resist and etched silicon, respectively.

The parameters mentioned above were tested systematically, and eventually resists without any visible cracking were produced. The following list summarizes how the different parameters influenced the degree of resist cracking:

- **Baking time and temperature:** This was found to be the most important aspect for avoiding resist cracking. According to th CSAR-62 data sheet [60], the baking should be done on a hot plate at 150 °C for 1 min. These were the baking parameters used initially. However, it turned out that the hotplate held a temperature approximately 15 °C lower than the set value. Therefore, the hotplate temperature was set to 165 °C, which was measured to give an actual temperature of 150 °C. This significantly decreased the degree of resist cracking. When in addition increasing the baking time to 3 min, resists without any visible cracking were produced.

- **Rounding of edges:** A significant improvement of the resist cracking issue was also achieved by rounding of sharp edges in the resist pattern. However, with the conventional baking time and temperature, still some cracking was observed.

- **Spacing between neighboring waveguides:** Initially, samples with $30\,\mu m$ and $60\,\mu m$ spacing between adjacent waveguides were fabricated. More cracking were observed in the latter case. This was also confirmed later, by fabricating features with 30 and 60 µm spacing on the same sample.

To summarize the effect of the three parameters above on the degree of resist cracking, increasing the baking time and temperature turned out to be the most important. Even with sharp edges and $60\,\mu m$ spacing between neighboring waveguides, crack-free resists were produced. Nevertheless, to be sure, rounding of sharp edges in the mask design is recommended. Regarding the spacing between waveguides, a larger spacing is beneficial when optically testing the samples. Therefore, the spacing between waveguides should be what is most practical for optical testing, but should be kept in mind if cracking issues arise.

Bulk and Sleeve

During initial fabrication iterations, bulk and sleeve exposure, as described in Section 3.3.2, were tested. On some samples, considerable alignment errors were observed, as can be seen in Figure 4.9. The PhC holes and the part of the waveguide just next to them are exposed as a sleeve, while the rest of the waveguides is treated as bulk. One can clearly see misalignment in the x-direction, and also a slight misalignment in the y-direction.

During a bulk and sleeve exposure, the current is changed during the exposure process. It is therefore crucial to give the system sufficient time after a current change for the current to stabilize. A waiting time of 45 min should be sufficient, and was used for the sample displayed in Figure 4.9. The only difference in the fabrication process between this sample and similar samples without alignment error, is that for the one with error, the bulk current was set 45 min before loading the sample, and exposure was started immediately after loading. For the sample without errors, a 45 min waiting step was included before the first exposure regardless of how much time the current had to stabilize before sample loading. Based on this, the probable cause for the different results is assumed to be temperature alteration when entering the isolated room where the EBL is located for loading the sample. The temperature in the EBL room is precisely controlled, and is not always exactly the same as the temperature in the surroundings. This may have caused some drift of the electron beam, which could explain the alignment error.
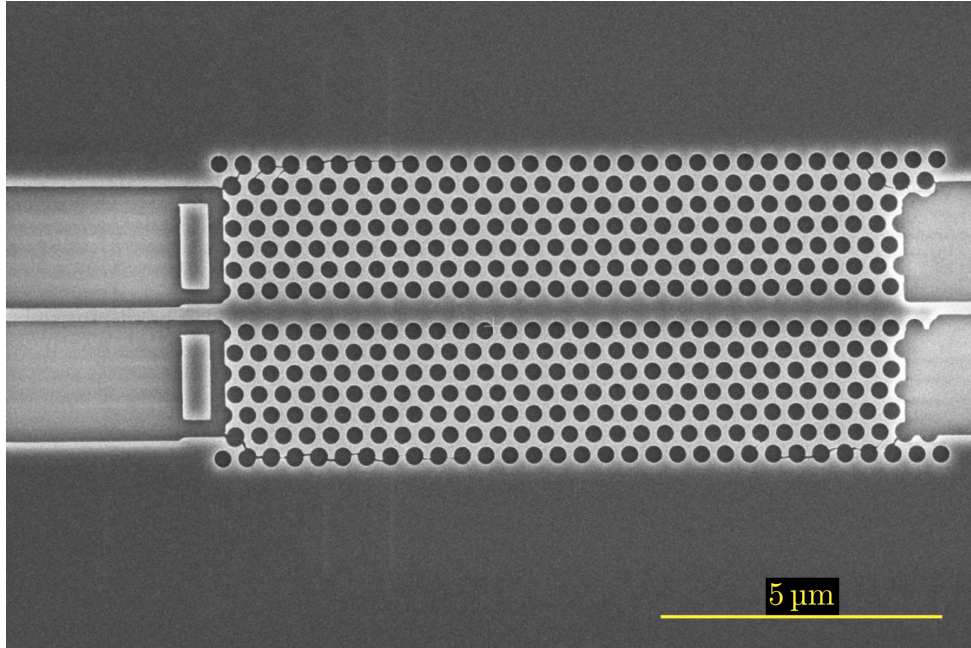
Figure 4.9: Alignment error from a bulk and sleeve exposure (1 pA and 5 nA). Image courtesy of Ingerid Hellen.

4.2.2 Hole Size

Due to electron scattering during EBL exposure, and possible anisotropy during etching, the physical sizes of exposed features become bigger than the corresponding features in the mask design. As a helpful tool for future processing of photonic crystals with the same process parameters presented here, Table 4.3 relates the real dimensions to the corresponding mask design sizes. Obviously, etched cylinders become bigger than intended, while waveguides (which are created by etching the surrounding material) become smaller than intended.

Table 4.3: Comparison of mask design sizes and actual sizes of fabricated features.

Component type	Mask design value [nm]	Physical value [nm]
Waveguide width	550	508
Cylinder radius (r)	129	114
Cylinder radius (R)	245	226
Cylinder radius (r^*)	77	68

4.2.3 Inverted Tapers

During fabrication of inverted tapers, some breaking of the tapers where they were the thinnest was observed. A suggested reason for this was too rough handling during development step and resist stripping. Therefore, the following points in the process recipe were modified:

- Blow-drying with nitrogen after development was excluded. The samples were instead left for some minutes to let the isopropanol evaporate.

- Stripping was done without using ultrasonic bath. The sample was simply placed in a beaker with the stripper solution, and left there for five minutes, with some slight stirring a few times during the process.

- If some CSAR62 was still left after the stripping step due to the exclusion of sonication, plasma cleaning was utilized to remove the last parts of resist. This was done for 3 minutes in an oxygen plasma with a plasma generator frequency of 20 kHz and an O_2 gas flow of 100 sccm.
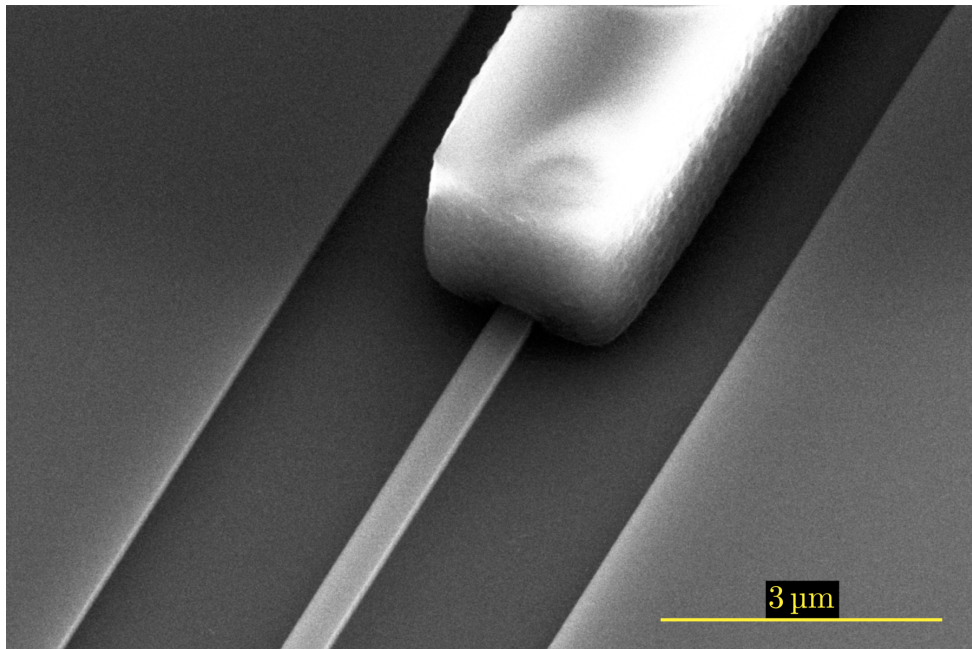

Figure 4.10: SEM-image of an SU-8 waveguide embedding a silicon waveguide.

Figure 4.10 shows an SU-8 waveguide embedding a silicon waveguide.

4.2.4 Final Fabrications

After multiple process iterations (15 samples were fabricated in total) with continuous adjustments, samples of very high quality were produced. Figure 4.11 shows SEM images at different magnification of two functioning transmission filters fabricated with the optimized process recipe, revealing very high quality and uniformity of the patterned silicon, with no signs of resist cracking. The transmission measurements presented in the next section confirmed that the quality of the fabricated devices was very good.

(a) H0 cavity, magnification: 12000.

(b) H0 cavity, magnification: 50000.

(c) H1 cavity, magnification: 12000.

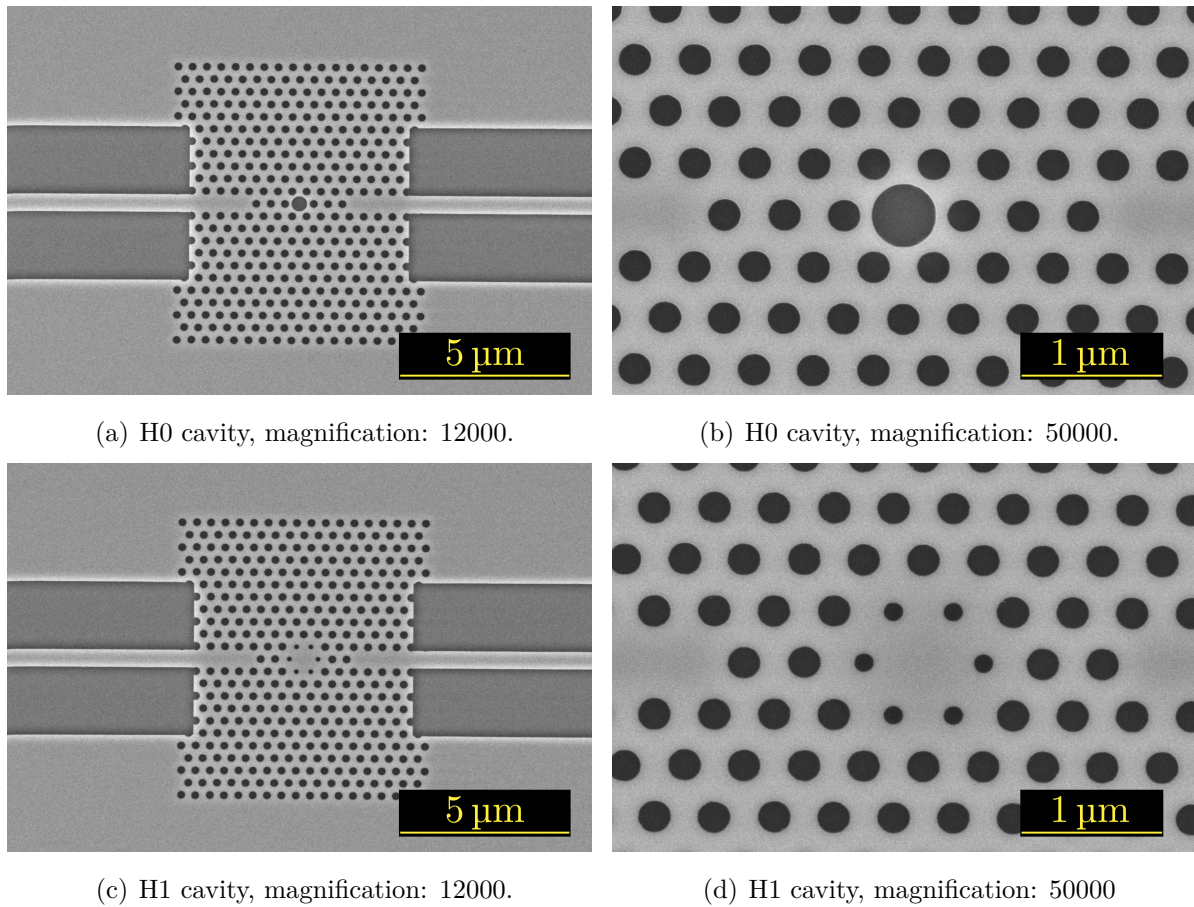(d) H1 cavity, magnification: 50000

Figure 4.11: SEM images of two functioning transmission filters, corresponding to the graphs in Figures 4.12(b) and 4.13.

4.3 Optical Characterization

4.3.1 Photonic Crystal Waveguide

Inverted Tapers

Using SU-8 waveguides for incoupling of light significantly enhanced the amount of light coupled into the silicon waveguide. Much lower amplification of the transmitted light was needed, meaning that the signal-to-noise ratio was improved. It is difficult to set exact numbers on the effect of having SU-8 waveguides, as the amount of transmitted light also depends on how well the sample is aligned, and the quality of the waveguide structures themselves. However, the amount of amplification needed to get the same signal strength as without SU-8 waveguides was for some samples at least ten times smaller than without SU-8 waveguides. The reason for this is partly small geometric overlap between the relatively big fiber compared to the silicon waveguide on the sample, and partly a RI mismatch between the two. When using a larger SU-8 waveguide, the geometrical mismatch is smaller, ensuring more light is coupled into the sample. It is also easier to align the input fiber to the "big" SU-8 waveguides than the "tiny" silicon waveguides.

4.3.2 Transmission Filter

Nearly all the different combinations of parameters resulted in functioning transmission filters. Figure 4.12 shows the transmission spectra obtained for two resonators of different geometry, one of each type (H0 and H1). Figure 4.14 shows IR-camera images of a resonance filter (H1) off and at the resonance wavelength. One can clearly see that light couples into the output waveguide in the case of resonance (4.14(b)), while there is no (or very little) coupling off the resonance frequency (4.14(a)). It is also observed that the scattering from the filter is more prominent off resonance, which makes perfectly sense, as the radiation is reflected and scattered by the filter to a larger degree than when it is coupled through the filter.

Q-factors of the two resonance peaks in Figure 4.12 were found to be 1187 and 753, for H0 and H1 filters, respectively. Comparing with simulations, it is surprising that the H0 filter yields a higher Q-factor than the H1 filter. One possible explanation could be that the resonance mode in the fabricated H0 filter actually is a monopole mode, which as discussed in Section 4.1.5, is expected to yield a higher Q-factor. The explanation could also be the other way around: The resonant mode in the H1 filter could be a

dipole mode. Since a dipole mode is doubly degenerate and the geometry of the cavity is not equal in the x-direction (along the waveguide) and in the y-direction, the resonance wavelengths of one dipole mode might be slightly shifted compared to the other, appearing as a broader resonance peak. Taking a closer look at the resonance peak for another H1 filter (Figure 4.13(b)), two peaks can actually be observed, supporting the suspicion of the resonant mode being degenerate with a slight shift between the resonances. The observed peak splitting could also be a result of fabrication disorder. However the mode-splitting behavior of H1 resonance cavities has been reported in literature, e. g. in Painter et al. [61], supporting this hypothesis. Luxmoore et al. [62] have reported a method to avoid the mode splitting by stretching or compressing the PhC lattice in only the x- or y-direction, and thereby obtaining a Q-factor of around 3300. Such fine-tuning of parameters was however not within the scope of this work, but is left as a suggestion for future work.

Comparing with the 3D simulation of the H0 filter (with $n_c = 4$), the Q-factor of the fabricated filter (with $n_c = 3$) is higher. Again, this could be explained by the resonant mode in the fabricated filter being a monopole mode. In addition, the 3D simulation was conducted in aqueous environment, altering the transmission characteristics. Based on the results from simulations, it is expected that fabricated filters with increased n_c will yield significantly higher Q-factors.

Comparing with the few reported results of cavity filters of similar geometry, the Q-factors found (especially for the H0 cavity) are of the order as the best reported values. For example, Gan and Li [63] reported a fabricated H0 cavity filter of similar geometry, yielding a Q-factor of 227.

An additional process step for improving the performance of the fabricated filters is to underetch the SiO$_2$ substrate. This would reduce the refractive index of the "substrate", from 1.33 (SiO$_2$) to 1.00 (air), resulting in better confinement (less loss) of the resonant modes. Leest et al. [64] report Q-factors of 1370 and 1750 for H0 and H1 cavities respectively, in underetched silicon. Comparing with these results, it becomes clear that the performance of the devices fabricated without underetching in this project is very good, especially for the H0 filter. Being able to fabricate transmission filters of sufficient quality to be used for biosensing without underetching would be highly beneficial, as the additional process step of underetching (involving use of hydrofluoric acid) is avoided.

(a) H0, $a = 410\,\mathrm{nm}$, $r = 0.27a$, $R = 0.54a$, $n_c = 3$.
Q=1187.

(b) H1, $a = 430\,\mathrm{nm}$, $r = 0.27a$, $r^* = 0.16a$, $n_c = 2$,
Q=753
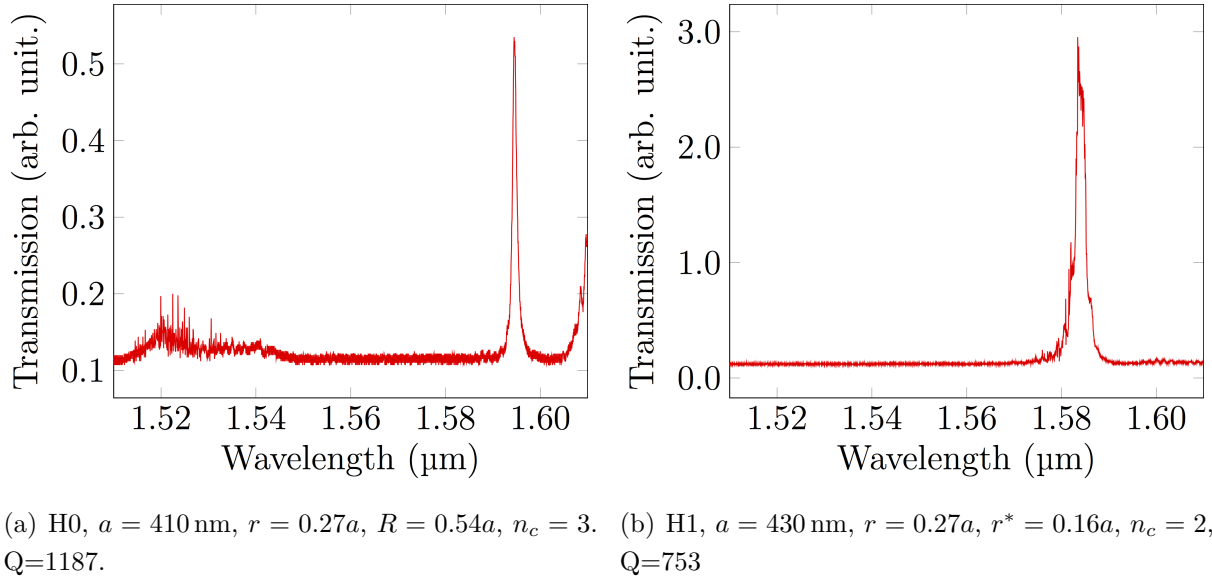
Figure 4.12: Transmission spectra for two fabricated photonic crystal transmission filters.

(a) H1, $a = 410\,\mathrm{nm}$, $r = 0.27a$, $r^* = 0.16a$

(b) Excerpt of the transmission spectrum in (a)
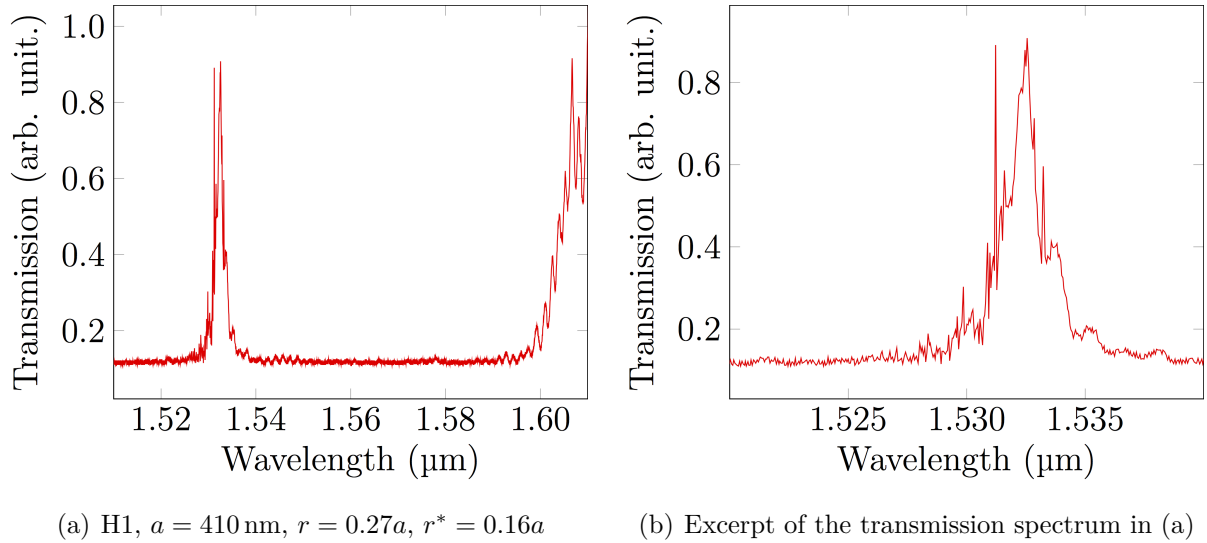
Figure 4.13: Transmission spectrum for a H1 filter, indicating splitting of the resonance peak.

(a) Off resonance

(b) At resonance

Figure 4.14: IR-camera image of a transmission filter (H1, $a = 430\,\text{nm}$, $r = 0.27a$, $r^* = 0.16a$), off resonance (a) (1583 nm) and at resonance (b) (1584 nm).

Chapter 5

Conclusion

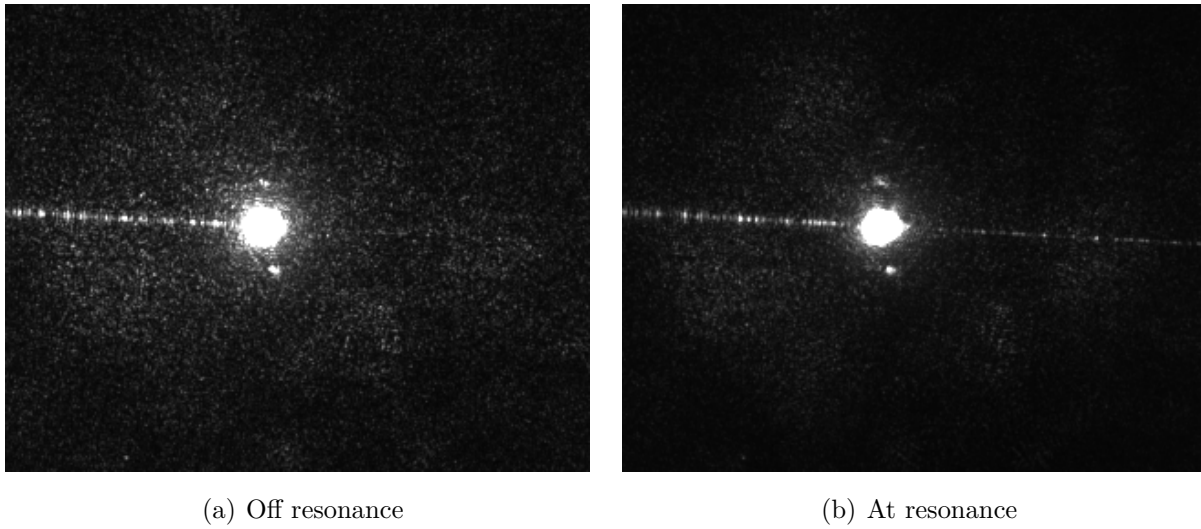The main objectives for this project have been to design, simulate and fabricate a functioning photonic crystal transmission filter, and investigate whether it is suitable for biosensing applications. In addition, a goal has been to further develop and optimize an existing fabrication process.

Simulations

All the photonic crystal structures investigated are based on a hexagonal pattern of air cylinders in a silicon slab. Initially, 2D simulations of bulk photonic crystals with MPB were performed to find values of the cylinder radius giving the most suitable properties in terms of photonic band gap and mode dispersion. In combination with simulations of linear defect waveguides with both MPB and MEEP, hole radii of $0.3a$ or smaller were found to be suitable. Further optimization of the waveguides can be done, but the waveguide design presented here proved to function when used as a component in transmission filters.

Different cavities (H0 and H1) were then introduced in the waveguides to create transmission filters. Both types of filters were simulated in two dimensions, and found to exhibit the desired ability of shifting the resonance frequency simply by tuning the geometry slightly. By increasing the number of holes on each side of the cavities along the waveguide (n_c), the Q-factor was found to increase significantly. The computed Q-factors were of the same order as the highest Q-factors reported in literature for similar filter designs.

The possibility for using the transmission filters for biosensing was investigated through 3D simulations. The H0 cavity filter exhibited a resonance frequency shift of around 1 nm when a biolayer was applied to the top surface. Interestingly, applying a biolayer to the

69

top surface rather than the inside of the cylinders resulted in a larger shift. It is therefore believed that the complex process of functionalizing the cylinders walls could be avoided, which would make the biosensors easier to produce.

Fabrication

Through many fabrication iterations, some process parameters have been optimized and documented to produce devices of better quality. Initial fabrications revealed severe cracking of the photonic crystal structures. By systematically investigating the lithography process, it was found that the time and temperature during the baking step were insufficient. Eventually, resonance filters of good quality and uniformity were fabricated and optically tested. Both H0 and H1 cavity filters exhibited transmission spectra with well defined resonance peaks, with estimated Q-factors of 1187 and 753, respectively, which are comparable to the best reported values of similar structures. It is believed that with further optimization of parameters, it should be possible to improve the Q-factors even more. In combination with simulation results, the results from testing of fabricated devices indicates that the photonic crystal transmission filters presented in this thesis are suitable for biosensing applications.

This was the first time that photonic crystal transmission filters were successfully fabricated at NTNU. This thesis provides designs and process recipes for fabricating well-performing transmission filters, which hopefully will be useful for future work in the ongoing lab-on-a-chip project.

Future Work

As the main objective for this work has been to fabricate a *functioning* transmission filter, extensive optimization of all design and process parameters have been outside the scope. There are numerous aspects that can be subject to optimization. In the following list, some significant points of improvement and suggestions for a continuation of this work are pointed out:

- To improve the performance of the transmission filters, further optimization could be done on linear defect waveguide design.

- A larger variety of parameters of the transmission filters should be tested, both through simulations (which would require more computational power than have been available in this work), and, more importantly, through fabrication.

- The fabrication process could be improved to yield devices of higher quality. For example, bulk and sleeve exposure could be utilized.

- Most importantly, the performance of the fabricated transmission filters as biosensors should be tested, by functionalization with binding agents and application of solutions containing relevant biomarkers.

Bibliography

[1] Størk Avelsgaard Lien. "Simulations of a Silicon Photonic Crystal Transmission Filter for Biosensing". Project Thesis. NTNU, 2017.

[2] Lars Grønmark Holmen. "Simulation and Fabrication of a Photonic Crystal Mach-Zehnder Interferometer". Master's Thesis. NTNU, 2016.

[3] Mia Othelie Stein. "Simulations and Fabrication of Photonic Crystal Waveguides and a Computational Study of Two-Dimensional Photonic Crystal Cavity Resonators". Master's Thesis. NTNU, 2018.

[4] Hakan Inan et al. "Photonic crystals: emerging biosensors and their promise for point-of-care applications". In: *Chem. Soc. Rev.* 46 (2 2017), pp. 366–388. DOI: `10.1039/C6CS00206D`.

[5] Xudong Fan et al. "Sensitive optical biosensors for unlabeled targets: A review". In: *Analytica Chimica Acta* 620.1 (2008), pp. 8 –26. ISSN: 0003-2670. DOI: `https://doi.org/10.1016/j.aca.2008.05.022`.

[6] Mindy Lee and Philippe M. Fauchet. "Two-dimensional silicon photonic crystal based biosensing platform for protein detection". In: *Opt. Express* 15.8 (2007), pp. 4530–4535. DOI: `10.1364/OE.15.004530`.

[7] Nina Skivesen et al. "Photonic-crystal waveguide biosensor". In: *Opt. Express* 15.6 (2007), pp. 3169–3176. DOI: `10.1364/OE.15.003169`.

[8] Frank Vollmer and Lan Yang. "Label-free detection with high-Q microcavities: a review of biosensing mechanisms for integrated devices". In: *Nanophotonics* 1.3-4 (Dec. 2012), pp. 267–291. ISSN: 2192-8614.

[9] John D. Joannopoulos et al. *Photonic Crystals: Molding the Flow of Light. second edition.* Ed. by Princeton University Press. 2008. ISBN: 9780691124568.

[10] P.C. Hemmer. *Kvantemekanikk: P.C. Hemmer.* Tapir akademisk forlag, 2005. ISBN: 9788251920285.

[11]   R. P. Feynman, R. B. Leighton, and M. L. Sands. *The Feynman lectures on physics.* Vol. 3. Reading, Mass. : Addison-Wesley Pub. Co., c1963-1965., 1963. Chap. 49.

[12]   B.E.A. Saleh and M.C. Teich. *Fundamentals of Photonics.* Wiley Series in Pure and Applied Optics. Wiley, 2007. ISBN: 9780471358329.

[13]   C. Kittel. *Introduction to Solid State Physics.* Wiley, 2004. ISBN: 9780471415268.

[14]   Toshihiko Baba et al. "Light localizations in photonic crystal line defect waveguides". In: *IEEE Journal on Selected Topics in Quantum Electronics* 10.3 (May 2004), pp. 484–491. ISSN: 1077-260X. DOI: 10.1109/JSTQE.2004.829201.

[15]   O. Painter, J. Vučković, and A. Scherer. "Defect modes of a two-dimensional photonic crystal in an optically thin dielectric slab". In: *J. Opt. Soc. Am. B* 16.2 (1999), pp. 275–285. DOI: 10.1364/JOSAB.16.000275.

[16]   A. D'Orazio et al. "Photonic Crystal Drop Filter Exploiting Resonant Cavity Configuration". In: *IEEE Transactions on Nanotechnology* 7.1 (2008), pp. 10–13. ISSN: 1536-125X. DOI: 10.1109/TNANO.2007.913427.

[17]   Safia Arafa et al. "High sensitive photonic crystal multiplexed biosensor array using H0 sandwiched cavities". In: *EPJ Web Conf.* 139 (2017), p. 00003. DOI: 10.1051/epjconf/201713900003.

[18]   C. Weisbuch and J. G. Rarity. *Microcavities and Photonic Bandgaps: Physics and Applications.* Ed. by John Rarity and Claude Weisbuch. Dordrecht: Springer Netherlands, 1996. ISBN: 978-94-009-0313-5. DOI: 10.1007/978-94-009-0313-5_1.

[19]   P. Meystre and M. Sargent III. *Elements of Quantum Optics.* 4th ed. Springer, 2007. ISBN: 978-3-540-74209-8. DOI: 10.1007/978-3-540-74211-1.

[20]   Ahmed Touhami. "Biosensors and Nanobiosensors, Design and Applications". In: Nanomedicine; One Central Press (OCP): Cheshire, UK, 2014. Chap. 15, pp. 374–403. ISBN: 978-1-910086-01-8.

[21]   Aaron J. Danner. *An introduction to the plane wave expansion method for calculating photonic crystal band diagrams.* Accessed on 2018-05-20. URL: https://www.ece.nus.edu.sg/stfpage/eleadj/planewave.htm.

[22]   A. Taflove and S.C. Hagness. *Computational Electrodynamics: The Finite-difference Time-domain Method.* Artech House Antennas and Prop. Artech House, 2005. ISBN: 9781580538329. URL: https://books.google.no/books?id=n2ViQgAACAAJ.

[23] Gouri Dhatt, Gilbert Touzot, and Emmanuel Lefrançois. "Approximations with Finite Elements". In: *Finite Element Method*. John Wiley and Sons, Inc., 2012, pp. 21–95. ISBN: 9781118569764. DOI: 10.1002/9781118569764.ch1.

[24] Sharee J. McNab, Nikolaj Moll, and Yurii A. Vlasov. "Ultra-low loss photonic integrated circuit with membrane-type photonic crystal waveguides". In: *Opt. Express* 11.22 (2003), pp. 2927–2939. DOI: 10.1364/OE.11.002927.

[25] W. Bogaerts and S.K. Selvaraja. "13 - Silicon-on-insulator (SOI) technology for photonic integrated circuits (PICs)". In: *Silicon-On-Insulator (SOI) Technology*. Ed. by Oleg Kononchuk and Bich-Yen Nguyen. Woodhead Publishing, 2014, pp. 395 – 434. ISBN: 978-0-85709-526-8. DOI: https://doi.org/10.1533/9780857099259.2. 395.

[26] Koji Yamada. "Silicon Photonics II - Components and Integration". In: ed. by David J. Lockwood & Lorenzo Pavesi. Springer-Verlag Berlin Heidelberg, 2011. Chap. 1, pp. 1–29. ISBN: 978-3-642-10505-0. DOI: 10.1007/978-3-642-10506-7.

[27] David Thomson et al. "Roadmap on silicon photonics". In: *Journal of Optics* 18.7 (2016), p. 073003. DOI: 10.1088/2040-8978/18/7/073003.

[28] Shiyang Zhu, G. Q. Lo, and D. L. Kwong. "Low-loss amorphous silicon wire waveguide for integrated photonics: effect of fabrication process and the thermal stability". In: *Opt. Express* 18.24 (2010), pp. 25283–25291. DOI: 10.1364/OE.18.025283.

[29] W.B. THOMPSON. "Chapter 1 - An Introcuction to Plasma Physics". In: *An Introduction to Plasma Physics (Second Edition)*. Ed. by W.B. Thompson. Second Edition. Pergamon, 1962, pp. 1 –8. ISBN: 978-0-08-011180-3. DOI: https://doi. org/10.1016/B978-0-08-011180-3.50004-7.

[30] M. Quirk and J. Serda. *Semiconductor Manufacturing Technology*. Prentice Hall, 2001. ISBN: 9780130815200.

[31] Carlos E. Viana et al. "Analysis of SiO2 Thin Films Deposited by PECVD Using an Oxygen-TEOS-Argon Mixture". en. In: *Brazilian Journal of Physics* 31 (June 2001), pp. 299 –303. ISSN: 0103-9733. DOI: 10.1590/S0103-97332001000200023.

[32] Nezih Pala and Mustafa Karabiyik. "Electron Beam Lithography (EBL)". In: *Encyclopedia of Nanotechnology*. Ed. by Bharat Bhushan. Dordrecht: Springer Netherlands, 2012, pp. 718–740. ISBN: 978-90-481-9751-4. DOI: 10.1007/978-90-481-9751-4_344.

[33] *STS-Elionix webpage.* URL: http://www.sts-elionix.com/.

[34] Fouad Karouta. "A practical approach to reactive ion etching". In: *Journal of Physics D: Applied Physics* 47.23 (2014), p. 233501. DOI: 10.1088/0022-3727/47/23/233501.

[35] Ray F. Egerton. "An Introduction to Microscopy". In: *Physical Principles of Electron Microscopy: An Introduction to TEM, SEM, and AEM.* Boston, MA: Springer US, 2005, pp. 1–25. ISBN: 978-0-387-26016-7. DOI: 10.1007/0-387-26016-1_1.

[36] Steven G. Johnson and J. D. Joannopoulos. "Block-iterative frequency-domain methods for Maxwell's equations in a planewave basis". In: *Opt. Express* 8.3 (2001), pp. 173–190. DOI: 10.1364/OE.8.000173.

[37] S.G. Johnson. *Notes on Perfectly Matched Layers.* Lecture Notes. Massachusetts Institute of Technology. 2010.

[38] Steven G Johnson. *Harminv Webpage.* Accessed on 2017-11-05. URL: http://ab-initio.mit.edu/wiki/index.php?title=Harminv.

[39] Vladimir A. Mandelshtam and Howard S. Taylor. "Harmonic inversion of time signals and its applications". In: *The Journal of Chemical Physics* 107.17 (1997), pp. 6756–6769. DOI: 10.1063/1.475324.

[40] Allen Taflove, A Oskooi, and S G. Johnson. *Advances in FDTD Computational Electrodynamics: Photonics and Nanotechnology.* Jan. 2013. ISBN: 978-1-60807-170-8.

[41] *COMSOL Multiphysics® v. 5.2.* URL: www.comsol.com.

[42] Mikhail N. Polyanskiy. *Refractive index database.* Accessed on 2017-10-20. URL: https://refractiveindex.info.

[43] Hiroyuki Takagi et al. "High Q H1 photonic crystal nanocavities with efficient vertical emission". In: *Opt. Express* 20.27 (2012), pp. 28292–28300. DOI: 10.1364/OE.20.028292.

[44] R.P.H. Kooyman, Jan Greve, and R.G.C. Oudshoorn. "Refractive index and layer thickness of an adsorbing protein as reporters of monolayer formation". In: 284.285 (1996), pp. 836–840. DOI: 10.1016/S0040-6090(95)08459-2.

[45] Huimin Ouyang, Christopher C. Striemer, and Philippe M. Fauchet. "Quantitative analysis of the sensitivity of porous silicon optical biosensors". In: *Applied Physics Letters* 88.16 (2006), p. 163108. DOI: 10.1063/1.2196069.

[46]   *WieWeb Software webpage*. URL: `http://www.wieweb.com/ns6/index.html`.

[47]   *GenISys Beamer webpage*. URL: `https://www.genisys-gmbh.com/web/products/beamer.html`.

[48]   *GenISys Tracer webpage*. URL: `https://www.genisys-gmbh.com/web/products/tracer.html`.

[49]   John Canny. "A computational approach to edge detection". In: *IEEE TRANSACTIONS ON PATTERN ANALYSIS AND MACHINE INTELLIGENCE* (1986).

[50]   Caroline A Schneider, Wayne S Rasband, and Kevin W Eliceiri. "NIH Image to ImageJ: 25 years of image analysis". In: *Nature Methods* 9 (June 2012), pp. 671–. DOI: `10.1038/nmeth.2089`.

[51]   Jens Høvik and Astrid Aksnes. "A study of approximations for accurate two-dimensional simulations of photonic components". In: *Advanced Photonics 2016 (IPR, NOMA, Sensors, Networks, SPPCom, SOF)* (2016), JTu4A.7.

[52]   Min Qiu. "Effective index method for heterostructure-slab-waveguide-based two-dimensional photonic crystals". In: *Applied Physics Letters* 81.7 (2002), pp. 1163–1165. DOI: `10.1063/1.1500774`.

[53]   C. Monat et al. "Slow Light Enhanced Nonlinear Optics in Silicon Photonic Crystal Waveguides". In: *IEEE Journal of Selected Topics in Quantum Electronics* 16.1 (2010), pp. 344–356. ISSN: 1077-260X. DOI: `10.1109/JSTQE.2009.2033019`.

[54]   Lars G. Holmen. *Simulations of Photonic Crystal Mach-Zehnder Interferometers for Biosensing Applications*. Project Report. Norwegian University of Science and Technology. 2015.

[55]   M. Notomi et al. "Structural tuning of guiding modes of line-defect waveguides of silicon-on-insulator photonic crystal slabs". In: *IEEE Journal of Quantum Electronics* 38 (July 2002), pp. 736–742. DOI: `10.1109/JQE.2002.1017583`.

[56]   Marko Lončar, Jelena Vučković, and Axel Scherer. "Methods for controlling positions of guided modes of photonic-crystal waveguides". In: *J. Opt. Soc. Am. B* 18.9 (2001), pp. 1362–1368. DOI: `10.1364/JOSAB.18.001362`.

[57]   René Matzen, Jakob S. Jensen, and Ole Sigmund. "Topology optimization for transient response of photonic crystal structures". In: *J. Opt. Soc. Am. B* 27.10 (2010), pp. 2040–2050. DOI: `10.1364/JOSAB.27.002040`.

[58] H. Y. Ryu and M. Notomi. "Enhancement of spontaneous emission from the resonant modes of a photonic crystal slab single-defect cavity". In: *Opt. Lett.* 28.23 (2003), pp. 2390–2392. DOI: `10.1364/OL.28.002390`.

[59] Sanja Zlatanovic et al. "Photonic crystal microcavity sensor for ultracompact monitoring of reaction kinetics and protein concentration". In: *Sensors and Actuators B: Chemical* 141.1 (2009), pp. 13 –19. ISSN: 0925-4005. DOI: `https://doi.org/10.1016/j.snb.2009.06.007`.

[60] *Positive E-Beam Resists AR-P 6200 (CSAR 62) Datasheet.* ALLRESIST. 2017. URL: `http://www.allresist.com/wp-content/uploads/sites/2/2016/12/allresist_produktinfos_ar-p6200_englisch.pdf`.

[61] O. Painter, J. Vučković, and A. Scherer. "Defect modes of a two-dimensional photonic crystal in an optically thin dielectric slab". In: *J. Opt. Soc. Am. B* 16.2 (1999), pp. 275–285. DOI: `10.1364/JOSAB.16.000275`.

[62] Isaac Luxmoore et al. "Restoring mode degeneracy in H1 photonic crystal cavities by uniaxial strain tuning". In: *Applied Physics Letters* 100 (Mar. 2012).

[63] Lin Gan and ZhiYuan Li. "Photonic crystal cavities and integrated optical devices". In: *Science China Physics, Mechanics & Astronomy* 58.11 (2015), p. 114203. ISSN: 1869-1927. DOI: `10.1007/s11433-015-5724-1`.

[64] Thijs van Leest et al. "Photonic crystal cavities for resonant evanescent field trapping of single bacteria". In: *Proc.SPIE* 8427 (2012), pp. 8427 –8427 –11. DOI: `10.1117/12.922746`.

[65] R. Kent Dybvig. *The Scheme Programming Language.* 4th ed. MIT Press, 2009.

[66] S. G. Johnson. *MIT Photonic Bands webpage.* URL: `http://ab-initio.mit.edu/wiki/index.php?title=MIT_Photonic_Bands`.

[67] S. G. Johnson. *MIT Electromagnetic Equation Propagation webpage.* URL: `http://ab-initio.mit.edu/wiki/index.php/Meep_Tutorial`.

Appendices

Appendix A

Linear Defect Waveguide Simulation With MPB

An example code for computing the defect bands in a linear defect waveguide is given below. Comments (green) should explain the purpose of each code line.

```
;constants regarding geometry:
(define-param a 1); lattice parameter
(define-param A (/ (sqrt 3) 2)); distance between rows in
    y-direction
(define-param r 0.3); hole radius
;dielectric constants and materials:
(define-param eps_silicon 8.10); epsilon for silicon

(define si (make dielectric (epsilon eps_silicon)))

(set! num-bands 50); how many eigenmodes to calculate
(set! default-material si); we want air holes in si background
;defining the supercell:
(set! geometry-lattice (make lattice (size 1 25 no-size)
        (basis1 1 0)
        (basis2 0.5 (/ (sqrt 3) 2))))
;set the unit cell geometry:
(set! geometry (list (make cylinder (center 0 0 0) (material air)
(radius r) (height infinity))))
;duplicate the air cylinders across the entire supercell:
(set! geometry
        (append
                (geometric-objects-lattice-duplicates geometry)))
;covering the central hole of the supercell:
```

```scheme
(set! geometry
        (list
                (make cylinder (center 0 0 0) (material si)
                    (radius r) (height infinity)))))

;defining k-points:
(set! k-points (list (vector3 0 0 0); Gamma
                     (vector3 0.5 0 0))); K
(set! k-points (interpolate 16 k-points)); how many values to
   interpolate for between the k-points
(set! resolution 32); creates a 32x32 computational grid for each
   lattice unit.


(run-te); calculate TE bands
```

In addition to running the code above, with a missing hole in the middle of geometry, another run without the defect was run with the same parameters, to obtain the continuum of projected bands from a defect-free crystal, as described in Section 3.2.3.

MPB code is written in the programming language Scheme [65], and saved in control (.ctl) files. For example, for a control file `waveguide.ctl` with the code, the simulation is run by calling `unix% mpb waveguide.ctl >& waveguide.out`. This produces a text file (`waveguide.out`) with the simulation results, which in the example code above consist of the TE bands, as asked for in the `run` command in the last code line.

The code is built in in the following way:

- Defining the parameters, such as sizes and material constants. In MPB, all sized are defined relative to the lattice constant, which by default is equal to 1.

- Specifying the basis vectors of the unit cell of the lattice, and defining the "supercell", a new "unit" cell containing the defect.

- Specifying the geometry.

- Defining symmetry points in the reciprocal lattice.

- Specifying resolution.

- Running the simulation, which calculates TE and/or TM bands.

The code example above calculated the first 50 bands of a linear waveguide in a hexagonal structure of air holes in silicon. The reason for calculating as much as 50 bands is that for each unit cell within the supercell (which is set to 1×25), the bands get folded back.

For more information on installation, and a thorough tutorial with more code examples, the reader is referred to the MPB webpage [66].

Appendix B

Transmission Filter Simulation With MEEP

The following code computes the transmission through a H1 filter in a two-dimensional model.

```
;constants regarding geometry:
(define-param a 1); lattice parameter
(define-param A (/ (sqrt 3) 2)); distance between rows in
    y-direction
(define-param r 0.3); hole radius
(define-param r3 0.18); radius of holes surounding the cavity
(define-param wg_width (- (* 2 A) (* 2 r))); width of strip
    waveguide
(define-param wg_length (* 2 a)); length of strip waveguide
(define-param pml_t 1); thickness of PML
(define-param flux_sep 0.5); distance from right flux plane to PML
(define-param source_sep 0.25); distance from source plane to PML
(define-param numx 17); number of periods along x
(define-param numy 15); number of periods along y
(define-param sx (+ (* a numx) (* 2 wg_length) (* 2 pml_t)));
    size of domain in x-direction
(define-param sy (+ (* numy A) (* 2 pml_t))); size of domain in
    y-direction
(define-param flux_pos_x (- (/ sx 2) (+ pml_t flux_sep)));
    position of the transmission flux plane
(define-param source_pos_x (- (/ sx 2) (+ pml_t source_sep)));
    position of the source plane
(define-param ref_run false); reference run or not
```

```scheme
;source properties:
(define-param fcen 0.2625); pulse center frequency
(define-param df 0.011); pulse width
(define-param nfreq 2000); number of frequencies to compute flux
   for

;simulation domain:
(set! geometry-lattice (make lattice (size sx sy no-size)));

;dielectric constants and materials:
(define-param eps_silicon 8.10); epsilon for silicon
(define si (make dielectric (epsilon eps_silicon)))
(set! default-material air); air environment

;simulation geometry:
;si slab if not reference run. waveguide if reference run
(if ref_run
(set! geometry (list
(make block (center 0 0 0) (material si) (size infinity wg_width
   infinity)))))
(if (not ref_run)        (set! geometry (list
(make block (center 0 0 0) (material si) (size numx numy
   infinity)))))

;air holes:
(if (not ref_run)
(set! geometry (append geometry
(geometric-objects-duplicates (vector3 (* 0.5 a) A 0) (-(+ numx))
   (+ numx 1)
(geometric-object-duplicates (vector3 (* 0.5 a) (- (+ A)) 0) (-
   (+ numx 1)) (+ numx 1)
(make cylinder (center 0 0 0) (radius r) (height infinity)
   (material air)))))))

;cover central row with silicon:
(if (not ref_run)
(set! geometry
```

```scheme
(append geometry
(list (make block (center 0 0 0) (material si) (size numx (* 2 r)
   infinity))))))

;adding holes along the waveguide, adjecent to cavity:
(if (not ref_run)
(set! geometry
(append geometry
(geometric-object-duplicates (vector3 a 0 0) -3 -1
(make cylinder (center 0 0 0) (radius r) (height infinity)
   (material air)))
(geometric-object-duplicates (vector3 a 0 0) 1 3
(make cylinder (center 0 0 0) (radius r) (height infinity)
   (material air))))))

;decrease hole radius around cavity:
(if (not ref_run)
(set! geometry
(append geometry (list
(make cylinder (center 1 0 0) (radius r) (height infinity)
   (material si))
(make cylinder (center -1 0 0) (radius r) (height infinity)
   (material si))
(make cylinder (center -0.5 A 0) (radius r) (height infinity)
   (material si))
(make cylinder (center -0.5 (* A -1) 0) (radius r) (height
   infinity) (material si))
(make cylinder (center 0.5 A 0) (radius r) (height infinity)
   (material si))
(make cylinder (center 0.5 (* A -1) 0) (radius r) (height
   infinity) (material si))
(make cylinder (center 1 0 0) (radius r3) (height infinity)
   (material air))
(make cylinder (center -1 0 0) (radius r3) (height infinity)
   (material air))
(make cylinder (center -0.5 A 0) (radius r3) (height infinity)
   (material air))
```

```scheme
(make cylinder (center -0.5 (* A -1) 0) (radius r3) (height
    infinity) (material air))
(make cylinder (center 0.5 A 0) (radius r3) (height infinity)
    (material air))
(make cylinder (center 0.5 (* A -1) 0) (radius r3) (height
    infinity) (material air))))))

;defining input and output waveguide:
(if (not ref_run)
(set! geometry
(append geometry
(list
(make block (center (/ (+ pml_t wg_length numx) -2)0 0) (material
    si) (size (+ pml_t wg_length) wg_width infinity))
(make block (center (/ (+ pml_t wg_length numx) 2)0 0) (material
    si) (size (+ pml_t wg_length) wg_width infinity))))))

;defining the resolution and PML layer
(set-param! resolution 16); the default resolution is 10
(set! pml-layers (list (make pml (thickness pml_t))))

;defining the excitation current source
(set! sources (list
(make source (src (make gaussian-src (frequency fcen) (fwidth
    df)))
(component Ey) (center (* source_pos_x -1) 0 0)
(size 0 wg_width infinity)
)))

;defining symmetries
(set! symmetries
(list (make mirror-sym (direction Y) (phase -1))))

; defining the flux plane at the output waveguide for
    transmission plots
(define trans
(add-flux fcen df nfreq (make flux-region
```

```
(center flux_pos_x 0 0)
(size 0 (* wg_width 10) infinity)))))

(run-sources+
        (stop-when-fields-decayed 50 Ey (vector3 flux_pos_x 0 0)
            1e-5)
        (at-beginning output-epsilon))

(display-fluxes trans)
```

Simulations in MEEP are set up in a similar manner as simulations in MPB, but several additional parameters need to be defined. For example properties of the source, ports for measuring transmission, perfectly matched layers (PMLs) and conditions for terminating the simulations have to be defined.

It is necessary to somehow normalize the transmission to get meaningful numbers. This is done by first computing the transmission through a simple silicon strip waveguide of equal thickness as the PhC waveguide, and with the same source properties (a reference run). Then, the computed transmission of the transmission filter is divided by the values from the strip waveguide simulation. For the code above, which is stored in `h1.ctl`, this is done by setting the `ref_run` parameter to true, by calling `unix% ref_run=true h1.ctl & h1.out`.

If mirror symmetries exist in the structure, the computation times can be significantly reduced. In the code above, there is symmetry only in the y-direction. Depending on the resonant mode being even or odd, the symmetry phase is set to 1 or minus 1, respectively.

The simulations need to run for some time after the electromagnetic pulse is excited, as it takes some time for the resonance to build up in the cavity, and couple into the output waveguide and reach the port. Since this time depends largely in the properties of the resonance cavity, it is convenient to terminate the simulation when the output power reaches a threshold value compared to the maximum value, than specifying a run time directly. The simulations in the code above is terminated when the output power has a value of 10^{-5} times the maximum value. For 3D simulation, this threshold resulted in inconveniently long computation times, and were therefore run until the output power was 10^{-3} times the peak value.

For more documentation and examples, the reader is referred to the MEEP website [67].